The role of random vorticity stretching in tropical depression genesis

Hao Fu* and Morgan O'Neill
Department of Earth System Science, Stanford University

* email: haofu@stanford.edu

This is a preprint for EarthArXiv. The manuscript has been submitted to *Journal of the Atmospheric Sciences*. Subsequent versions may have slight modifications. The authors welcome feedbacks from anyone who reads the manuscript.

The role of random vorticity stretching in tropical depression genesis

Hao Fu* and Morgan O'Neill

Department of Earth System Science, Stanford University, California

**Corresponding author address:* Hao Fu, 473 Via Ortega, Stanford, CA 94305.

E-mail: haofu@stanford.edu

Generated using v4.3.2 of the AMS LaTeX template

ABSTRACT

Tropical deep convection plays a key role at the tropical depression stage of tropical cyclogenesis by aggregating vorticity, but no existing theory can depict such a stochastic vorticity aggregation process. Vorticity probability distribution function (PDF) is proposed as a tool to predict the horizontal structure and wind speed of the tropical depression, a tropical cyclone in its early stage. The reason lies in the tendency for a vortex to adjust to an axisymmetric and monotonic vorticity structure. Assuming deep convection as independent and uniformly distributed vortex tube stretching events in the lower troposphere, repetitive vortex tube stretching will make the air column area shrink many times and significantly increase vorticity. A theory of vorticity PDF is established by modelling the random stretching process as a Markov chain. The PDF turns out to be a weighted Poisson distribution, in good agreement with a randomly-forced divergent barotropic model (weak temperature gradient model), and in rough agreement with a cloud-permitting simulation. The result shows that a strong and sparse deep convective mode tends to produce more high vorticity air columns, which favors tropical cyclogenesis.

1. Introduction

The mechanism of tropical cyclogenesis remains a challenging scientific problem. The formation of a tropical cyclone might be loosely split into three stages: (i) the formation of a weak cyclonic region ("embryo region") where convection prefers to occur, (ii) the spin up of a cyclonic circulation in the embryo, and (iii) its intensification into a vortex with a self-sustaining eyewall updraft (Montgomery et al. 2006).

The embryo region usually takes the form of one or multiple mesoscale convective systems (MCS). It can be generated in an easterly wave trough (Gray 1998) and especially its intersection with the critical layer (Dunkerton et al. 2009), a large-scale confluence zone, a monsoon shear line (Ritchie and Holland 1999), a pair of mixed Rossby-gravity waves' cyclonic gyres (Ferreira et al. 1996), or perhaps spontaneously via the self-aggregation of deep convection (Wing et al. 2016; Holloway et al. 2017). The MCS provides a moist region which protects the convection inside from laterally entraining dry air. Its weak cyclonic circulation also protects convection from the environmental strain and provides some additional basic state background vorticity for convection to stretch (Dunkerton et al. 2009).

At the second stage, the updraft of deep convection produces a vertical vorticity anomaly in the middle troposphere due to vortex tube stretching and tilting (Montgomery et al. 2006). The convection usually dies in around an hour, but the vorticity remnant lasts far longer (Wissmeier and Smith 2011). The vorticity patches are further pushed inward by the mid level converging overturning circulation (Kilroy et al. 2017), which is driven by Ekman pumping, moisture and longwave radiation feedbacks (Smith 2000; Davis 2015). Montgomery et al. (2006) intuitively described it as 2D turbulence punctuated by 3D convective events. In about two days, the subsequent vortex merger spins up a tropical depression which is a quasi-circular vortex with a sustained maximum surface wind of up to 17 m s^{-1}, but generally free of eye (Charney and Eliassen 1964; Montgomery et al. 2006; AMS-Glossary 2012).

At the third stage, the deepened central pressure (corresponding to a high inertial stability core), Ekman pumping and the strong surface flux near the radius of maximum wind lead to a ring-like eyewall updraft, marking the maturity of the hurricane (Rotunno and Emanuel 1987; Emanuel 1997; Gray 1998). The middle layer contraction slows down due to the establishment of gradient wind balance, and the inflow enters mostly through the frictional boundary layer (Montgomery and Smith 2014).

We focus on the second stage, which is the spin up phase of the vortex, or in other words, the formation of tropical depression from an existing MCS. As for theoretical modelling, Charney and Eliassen (1964) studied the role of Ekman pumping in lifting parcels and releasing the stored conditional instability. Rotunno and Emanuel (1987) and Emanuel (1989) built an axisymmetric balanced model with a prognostic boundary layer moist entropy and angular momentum, which controls the free troposphere via convective quasi-equilibrium assumption. They argue that the wind-induced surface sensible and latent heat fluxes moisten the atmosphere, weaken downdrafts, and enhance updrafts as the wind grows to finite-amplitude. Raymond et al. (2007) used gross moist stability (Neelin and Held 1987) to link wind-induced surface heat flux to convergence and explored its competition with the wind-induced frictional spin down rate. All three models solve the axisymmetric mode or the even simpler system-averaged quantities. They do not include an important asymmetric effect: the aggregation of convectively generated eddies, which has been recognized as “vortical hot tower route” (Hendricks et al. 2004; Montgomery et al. 2006). Both the random nature of the convective forcing and the subsequent chaotic eddy motion limit the predictability of the major vortex’s intensity (Van Sang et al. 2008). In a simple barotropic view, it is the cooperation between the upscale growth of vorticity produced by transient convective forcing, as well as the inward advection by the system inflow induced by the convective ensemble (Kilroy et al. 2017). A quantitative model has not been established, probably due to the difficulty in parameterizing the radial eddy vorticity flux.

In this paper, we try another decomposition: the widening of vertical vorticity probability distribution function (PDF) through the repetitive random stretching and convergent transport by the short-lived convective clouds, and the rearrangement of the vorticity field into an axisymmetric and radially monotonic compact vortex by the eddies. We will show that the PDF evolution roughly obeys a Markov chain which yields an approximate analytical solution. The axisymmetric state may not be completely reached by the end of the second stage, but it sets an upper bound of maximum wind that can be reached in the axisymmetrization process. The complicated eddy dynamics only determines the axisymmetrization time scale and a modification of the PDF by turbulent mixing, which are probably less important. We employ a one-layer shallow water model to demonstrate it, with random local mass sink seeded into a circular region to mimic an existing MCS. This scheme, which has been used in a domain-homogeneous seeding mode, was first introduced by Vallis et al. (1997) and has been applied to study the formation of the Great Red Spot (Showman 2007), giant planets' polar vortex (O'Neill et al. 2015, 2016) and jet (Thomson and McIntyre 2016). To the authors' knowledge, the scheme has not been applied to tropical cyclogenesis where convection concentrates at a part of the domain, and its elegant statistical property as a Markov chain remains untouched.

The paper is organized in the following way. Section 2 introduces the simplified tropical depression genesis setup within a shallow water equation (SWE) and its further simplification to a weak temperature gradient model where the Markov chain is more strictly valid. Section 3 describes the numerical solver. Section 4 describes the flow evolution of the reference test. Section 5 presents a theory of the vorticity PDF. Section 6 validates the PDF model with sensitivity tests and discusses its link to vortex intensity. Section 7 further validates the theory with a cloud-permitting simulation of tropical cyclogenesis. Section 8 concludes the paper. The derivation of the continuous PDF equation and a list of mathematical symbols are presented in the supplemental material.

2. An idealized tropical depression genesis problem

a. The macroscopic setup

First, we present a more detailed review of the environment of tropical depression formation, which guides the design of a shallow water setup. An easterly wave trough that provides a cyclonic background relative vorticity is of $\sim$ 700 km scale (Gray 1998). It can embed multiple $\sim$ 250 km scale MCSs which are a mixture of aggregated stratiform and convective cloud (Gray 1998). According to Houze Jr et al. (2009), the convective region usually possesses a convectively-induced rotational core in the middle troposphere (Gray 1998), called a mesoscale convective vortex (MCV). An MCV usually lacks near-surface vertical vorticity, due to the divergence caused by the low-level ($<$ 2 km) evaporative cooling of precipitation falling from the stratiform region (Fritsch et al. 1994). If there is growth of low level vorticity, air-sea interaction feedback will be excited and the system will be on the track of tropical cyclogenesis.

The formation mechanism of low-level vorticity is still in debate. One explanation is the "top-down" development of the middle level vortex via vortex interaction (Ritchie and Holland 1997) or transport by evaporation-driven downdraft (Bister and Emanuel 1997). The other is the "bottom-up" mechanism. It emphasizes the production of low-level vorticity by the deep convective stretching of the MCV's vertical absolute vorticity which is small but nonzero at low-level (Montgomery et al. 2006). The deep convection is promoted by the moistening and cooling of the lower and middle level by the MCS' stratiform precipitation (Bell and Montgomery 2019).

In this paper, we focus on the vortex dynamics of the low-mid level ($\sim$ 1 to 6 km height) spun up by deep convective vorticity stretching within an MCS, which is the basis of the "bottom-up" view but largely remains descriptive. According to Kilroy et al. (2017), this is the level where most of the free tropospheric convergence occurs. The influence of the existing middle level relative vorticity, as well as the upward transport of boundary layer vorticity during Ekman pumping, are neglected. The low-mid level is modelled with a one-layer barotropic model. We seed the updrafts only in a circular "vigorous convection region" with a fixed radius of R ($\sim$ 100 km), to mimic a single MCS in a doubly periodic domain whose width is $L \sim 800$ km. A schematic diagram of this setup is presented in Fig. 1. During the spin up of a realistic tropical depression, the middle layer inflow that is characterized by the MCS region mean divergence δ_0 (negative) first grows due to higher tropospheric moisture and surface flux, and then decreases due to the build up of inertial stability (Kilroy et al. 2017). The δ_0 depends on the complicated interaction between convection and the vortex. For simplicity, we will use a fixed δ_0 in the theoretical model of vorticity PDF and all the one-layer model simulations. However, it will be shown that the PDF theory does not require this constraint: the time dependence of δ_0 can be absorbed into a nondimensional temporal coordinate which is rescaled with δ_0. This novel rescaling decouples the convective feedback from vortex dynamics to some extent.

b. The shallow water analogy for a stratified atmosphere

We follow Hendricks et al. (2014) to view the continuously stratified atmosphere as a one-layer isentropic model. The active layer represents the low-middle troposphere (roughly 1-6 km height), with a thickness of $H = 5$ km and a vertical temperature range of $\Delta\theta = 22.04$ K. It is capped by a static upper layer which denotes the upper troposphere. As the atmospheric lapse rate in the tropics is close to moist adiabatic, we set the reduced gravity as $g' = g\Delta\theta/\theta_{00} = 0.72$ m s^{-2}, with

$\theta_{00} = 300$ K denoting a reference potential temperature. The internal gravity wave phase speed is $c_0 = \sqrt{g'H} = 60$ m s^{-1}.

Ooyama (1969) presented a three-layer view of deep convection, which is recently updated by Schecter and Dunkerton (2009). Suppose the boundary layer detrains a thermal bubble. It releases latent heat, entrains some middle tropospheric air, and will rise to the upper troposphere if it is buoyant enough. For the even simpler one-layer setup, we let the low-mid level troposphere thickness sink due to the updraft be Q_u (negative, unit: m s^{-1}), which is proportional to diabatic heating in an isentropic coordinate. Parcels are assumed to slowly return from the upper to the low-mid layer through radiative cooling, which corresponds to a thickness source Q_{rad} (positive, unit: m s^{-1}). The continuity and momentum equations are:

$$\frac{\partial h}{\partial t} + \nabla \cdot (\mathbf{u}h) = Q_u + Q_{rad} + \nu \nabla^2 h, \tag{1}$$

$$\frac{\partial \mathbf{u}}{\partial t} + \mathbf{u} \cdot \nabla \mathbf{u} + f_0 \mathbf{k} \times \mathbf{u} = -g' \nabla h - \frac{\mathbf{u}}{\tau_d} + \nu \nabla^2 \mathbf{u}. \tag{2}$$

Here $\mathbf{u}$ is the horizontal velocity, h is layer thickness, f_0 is Coriolis parameter, $\nabla \equiv \mathbf{i}\partial/\partial x + \mathbf{j}\partial/\partial y$ is the horizontal gradient operator. For simplicity, we treat the Ekman spindown, as well as the vertical momentum transfer by both updraft (cumulus drag) and radiative cooling as a bulk linear Rayleigh drag whose time scale is τ_d. The ν is a constant diffusivity to suppress numerical instability. To be self-consistent with the omission of cumulus drag, an updraft is assumed to move with the middle layer wind. This is different from the shallow water models of Showman (2007) and O'Neill et al. (2016) who fix the updraft position in a convective event.

In the real atmosphere, as the vortex intensifies, the low-level horizontal vorticity could be tilted by the updraft to form vertical vorticity dipoles (Vallis et al. 1997). These, together with the vorticity monopoles produced by stretching, are both important for hurricane formation (Montgomery et al. 2006; Kilroy et al. 2014). What is more, the Ekman pumping causes divergence in the middle troposphere which can counteract part of the convection-induced inflow (Smith 2000). We will leave the careful consideration of these processes for future work.

c. The application of weak temperature gradient approximation

We propose that SWE can be further simplified to a weak temperature gradient (WTG) equation for understanding the vortex spin up at the early stage of tropical cyclogenesis. It is vital for establishing the vorticity PDF model in section 5.

The Coriolis force and the fluid inertia tend to invoke some pressure gradient to balance them. For slow motion at the low latitude where the Coriolis parameter is small, buoyancy anomaly cannot accumulate at the large scale. This leads to WTG approximation, where geostrophic adjustment is instantaneous and the continuity equation in SWE simplifies to the balance between mass sink and divergence (Sobel et al. 2001):

$$H\delta = Q_u + Q_{rad}. \tag{3}$$

Here $\delta = \nabla \cdot \mathbf{u}$ is horizontal divergence which is externally prescribed with convective and radiative parameterization. Dynamically, the potential vorticity degenerates to absolute vorticity $\omega_a = \omega + f_0$ (Sobel et al. 2001).

Enagonio and Montgomery (2001) have shown that there is little difference between a shallow water model and the nondivergent barotropic model ($\delta = 0$) for the free-evolving 2D vortex dynamics of an early stage hurricane vortex, primarily due to i) the small system length scale compared to Rossby deformation radius of the gravest mode, ii) the small Froude number Fr (definition shown below) and iii) the fast geostrophic adjustment compared to the axisymmetrization time scale (measured with strain rate). As the convergent flow is much weaker than the rotational flow, the criterion for WTG should be identical. The first two criteria which are more basic are stated in (4) and (5) respectively:

$$\mathrm{Bu} = \frac{R^2}{L_R^2} \ll 1, \quad \text{with} \quad L_R = \frac{\sqrt{g'H}}{f_0}, \tag{4}$$

$$\mathrm{Fr} = \frac{V_\theta}{\sqrt{g'H}} \sim \left(-\frac{h'}{H}\right)^{1/2} \ll 1, \tag{5}$$

where L_R is Rossby deformation radius, h' is the deviation of layer thickness from its basic state H, Fr is defined as the ratio of azimuthal wind scale V_θ to gravity wave speed c_0. Using $R = 100$ km and a low latitude Coriolis parameter $f_0 \sim 5 \times 10^{-5}$ s^{-1}, we get $L_R \sim 1200$ km and Bu $=$ $0.007 \ll 1$. The relation between Fr and $-h'/H$ in (5) is derived with cyclostrophic wind balance assumption, which is applicable to a strong tropical depression where Coriolis force is generally weaker than centrifugal acceleration. It is worth noting that gravity wave will be important to hurricane when it is coupled to convection (Lahaye and Zeitlin 2016).

The full WTG governing equation is introduced here. In the updraft region, the mass loss is balanced by convergence immediately; radiative cooling drives a slow divergent flow everywhere. The vertical vorticity equation is:

$$\frac{\partial \omega}{\partial t} + \mathbf{u} \cdot \nabla \omega = -\delta(\omega + f_0) - \frac{\omega}{\tau_d} + \nu \nabla^2 \omega. \tag{6}$$

The total velocity is a superposition of rotational wind and divergent wind:

$$\mathbf{u} = \mathbf{k} \times \nabla \psi + \nabla \phi, \quad \text{with} \quad \nabla^2 \psi = \omega,\ \nabla^2 \phi = \delta. \tag{7}$$

Here ψ is a stream function and ϕ is a velocity potential. They are linked to ω and δ through the two Poisson equations. The doubly-periodic boundary condition eliminates the harmonic component. Equations (3), (6) and (7) are the so-called weak temperature gradient approximation equation (WTGE). It is essentially a 2D barotropic vorticity equation punctuated by diabatic vorticity stretching, which involves both vorticity magnitude change and a convergent flow.

d. The convective representation

1) Formulation

We employ the random convection scheme of Showman (2007) in simulating convection on Jupiter to study the terrestrial tropical atmosphere. The convective mass loss rate (or equivalently the middle layer updraft speed increment with a minus sign) Q_u is represented as a sequence of Gaussian shape mass sinks Q_n (unit: m s^{-1}) that are isolated in time and space:

$$Q_u(\mathbf{x},t) = \sum_{n=1}^{+\infty} Q_n(\mathbf{x},t), \quad \text{with} \quad Q_n(\mathbf{x},t) = \widetilde{Q_m} e^{-\frac{|t-t_n|^2}{\widetilde{\tau_u}^2} - \frac{|\mathbf{x}-\mathbf{x_n}|^2}{\widetilde{r_u}^2}}. \tag{8}$$

For every Δt time, a new updraft is seeded to a random position in a circular area within a radius R which represents an MCS. The $\widetilde{Q_m}$ is the peak mass sink rate, $\widetilde{\tau_u}$ is a fixed updraft duration time scale which is controlled by the onset time of downdraft in the real atmosphere (Emanuel 1994), and $\widetilde{r_u}$ is a fixed updraft size parameter. The seeding time is a deterministic sequence: $t_n = n\Delta t$. The updraft center vector $\mathbf{x_n}$ moves with the local wind. It is calculated with the initial seeding position $\mathbf{x_{0n}}$ which is a random vector sequence with uniform distribution that satisfies $|\mathbf{x_{0n}}| < R$ (with the MCS center as the coordinate origin), as well as the local velocity: $\mathbf{x_n} = \mathbf{x_{0n}} + \int_{t_n}^{t} \mathbf{u}(\mathbf{x},t')\, dt'$.

The radiative cooling Q_{rad} (positive) is set as a spatially uniform but temporally fluctuating value that instantaneously balances Q_u to keep the domain average diabatic heating at zero:

$$Q_{rad} = -\frac{1}{L^2} \iint Q_u d\mathbf{x} \approx -\delta_0 H \frac{\pi R^2}{L^2}. \tag{9}$$

The fluctuation, which is manifested as the "$\approx$" in (9), converges to a constant value if there are enough clouds in the domain. For WTGE, the divergence induced by convective and radiative process obeys (3).

The diabatic heating that involves random factors leads to a set of stochastic differential equations. This convective scheme offers adjustable cloud parameters. For smaller updraft strength $\widetilde{Q_m}$

and seeding interval Δt, convection is more fine-grained and the limit is a purely axisymmetric and deterministic problem controlled by the convergence of an angular momentum ring.

Physically, the random updraft position mostly originates from the seemingly random boundary layer dry convection or cold pool collision (Würsch and Craig 2014; Haerter 2019; Torri and Kuang 2019). However, it is increasingly unsuitable as the major vortex develops, mainly in three aspects:

- The convective position should be allowed to follow the contracting high vorticity region which pumps more air out of the boundary layer. The coupling of convection to local vorticity is also needed to properly represent the convectively coupled vortex Rossby wave and its interaction with mean-flow (Wang 2002a,b).
- The convective strength near the vortex center should be allowed to be suppressed by the upper tropospheric warm core which is mainly induced by centrifugal acceleration (Schecter and Dunkerton 2009). This effect will be important when the layer thickness gradient is large (Fr is large).
- The middle layer entrainment might decrease as the environment spins faster (higher inertial stability). This is a robust behavior of dry rotating plumes but is still unclear for moist convection (Julien et al. 1999; Peters et al. 2020).

2) Statistical property

For convenience, we idealize the Gaussian updraft as a "mass-equivalent top-hat" with a mass-sink of $\widetilde{Q_m}$, radius $\widetilde{r_u}$ and duration time $\widetilde{T_u} = \pi^{1/2}\widetilde{\tau_u}$. We will introduce the "vorticity equivalent" top-hat in section 4a, which is an approximation to a sufficiently diffused "mass-equivalent top-hat". To distinguish between the two objects, the "$\sim$" is used to denote parameters related to "mass-equivalent top-hat". These parameters can be combined into two divergence scales, which are the divergence at an updraft δ_u (< 0), and the MCS mean divergence δ_0 (< 0) which is much smaller in magnitude:

$$\delta_u = \frac{\widetilde{Q_m}}{H}, \quad \delta_0 = \frac{\widetilde{Q_m}}{H}\frac{\widetilde{r_u}^2}{R^2}\frac{\widetilde{T_u}}{\Delta t}. \tag{10}$$

The statistically averaged time interval between the onset of two convective events at a fixed location (revisit time) is $\tau_{rev} = \Delta t R^2/\widetilde{r_u}^2$. It leads to two important nondimensional parameters:

- Nondimensionalizing τ_{rev} with δ_0 yields the convective intermittency parameter, which turns out to be the updraft accumulated convergence:

$$-\frac{\widetilde{\Delta h}}{H} = -\delta_0\tau_{rev} = -\frac{\widetilde{Q_m}\widetilde{T_u}}{H} = \frac{-\delta_0 \Delta t R^2}{\widetilde{r_u}^2}. \tag{11}$$

  Here $\widetilde{\Delta h} = \widetilde{Q_m}\widetilde{T_u}$ is the layer thickness change in an updraft. A higher $-\widetilde{\Delta h}/H$ means convection is in a more coarse-grained mode.

- The probability for any particular location to be under convection, or equivalently, the updraft fractional area is: $\sigma_u = \widetilde{T_u}/\tau_{rev} = \delta_0/\delta_u$. The σ_u is also the probability for the center of a new updraft to fall on the convective region, so it measures the potential of updraft interaction.

3. The numerical method and the reference test

The shallow water equation (SWE) which is defined in (1) and (2), as well as the weak temperature gradient equation (WTGE) which is defined in (3), (6) and (7) are solved on a doubly periodic square plane. The numerical solver is a MATLAB code developed by the first author. It uses standard spectral method, with zero padding technique to eliminate the aliasing error in product terms. The SWE solver uses the semi-implicit second order leapfrog time-stepping to stabilize the fast gravity wave, and the WTGE solver (without concerning gravity wave) uses the third order Runge-Kutta time-stepping which has higher temporal accuracy (Durran 2010).

In appendix A, we show that the SWE and WTGE can be fully nondimenisonalized. The WTGE is controlled by six nondimensional parameters: $-\delta_0/f_0$ measures the relative importance of rotational to convergent behavior, $-\widetilde{\Delta h}/H$ measures convective intermittency, $-\delta_0\widetilde{T_u}$ measures convective time scale, $\widetilde{r_u}/R$ measures the updraft size relative to the system size, $-\delta_0\tau_d$ measures the strength of drag and $\mathrm{Re} = f_0R^2/\nu$ measures the importance of horizontal viscosity. For the reference test, we set $-\delta_0/f_0 = 0.228$, $-\widetilde{\Delta h}/H = 8/5$, $-\delta_0\widetilde{T_u} = 0.04$, $\widetilde{r_u}/R = 0.08$, $-\delta_0\tau_d = \infty$ (no damping) and $\mathrm{Re} = 3116.7$. For the SWE, there is an additional $\mathrm{Bu} = R^2/L_R^2 = 0.007$.

A dimensional interpretation of the reference test is shown below. It corresponds to a domain width of $L = 800$ km, a 20°N Coriolis parameter $f_0 = 4.99\times10^{-5}$ s^{-1}, a system-averaged convergence $\delta_0 = -1.138\times10^{-5}$ s^{-1} ($-\delta_0^{-1} = 1.02$ days), a basic state layer thickness $H = 5$ km, an updraft total thickness sink $\widetilde{\Delta h} = -8$ km, an updraft duration time $\widetilde{\tau_u} = 2000$ s ($\widetilde{T_u} = 3544.9$ s) and an updraft radius $\widetilde{r_u} = 8$ km based on the estimation of Hendricks et al. (2004) and Montgomery et al. (2006), a MCS radius $R = 100$ km (Houze Jr et al. 2009) and a horizontal viscosity $\nu = 160$ m^2 s^{-1} which is approximately the lowest ν to guarantee numerical stability at current resolution (576×576 grid point in physical space, or a grid spacing of 1.39 km). Other parameters can be calculated from the settings above: $Q_m = -2.26$ m s^{-1}, $\Delta t = 900$ s, $\sigma_u = 0.025$. In numerical implementation, the integration time is 4 days, and the time step is 4.96 s. The Courant number estimated with a 30 m s^{-1} wind is 0.11. As the model is inherently stochastic, each test includes an ensemble of 20 runs.

We remark that $-\delta_0/f_0$ is regarded as a free parameter in this model. Physically, it depends on the complicated feedback between convection and the vortex circulation, and should at least depend on R and f_0. The current choice of δ_0 enables the system to exceed the 17 m s^{-1} tropical depression bound and reach the tropical storm stage in three days, which is not far from the 1-2 days growth time scale in the real world (Montgomery et al. 2006).

4. The flow evolution

We first consider the vorticity production process in a single updraft, and then move to the tropical depression genesis problem which involves multiple updrafts.

a. Single convection

A convective updraft induces a convergent flow that reduces the air column area, and increases the vorticity by stretching. In an updraft event with an accumulated convergence of $-\widetilde{\Delta h}/H$, the area of air involved in a stretching process shrinks from $\pi\widetilde{r_u}^2(1-\widetilde{\Delta h}/H)$ to $\pi\widetilde{r_u}^2$. The conservation of circulation shows that the average absolute vorticity within the influenced area changes from an initial value $\omega_{a,0}$ to $\omega_{a,0}(1-\widetilde{\Delta h}/H)$. Though the vorticity does not diminish after the updraft event, the size reduction induces a stronger horizontal diffusion that smooths the vorticity anomaly. In the vorticity PDF model, we are interested in the vorticity strength by the time it is hit by the next updraft, so a diffusion-correction should be implemented.

In appendix B, we use scale analysis to show that a significant smoothing does occur. We introduce a "vorticity-equivalent top-hat", which is a flatter version of the "mass-equivalent top-hat" that describes the shape of the vorticity patch seen by the next convection. The vorticity top-hat radius is set as $r_u = \alpha_r\widetilde{r_u}$ where α_r is a free parameter. The total absolute circulation within r_u is still conserved. In section 6a, we show that a fixed $\alpha_r = \sqrt{2}$ works well in the vorticity PDF model. We preliminarily explain the insensitivity as an automatic damping mechanism: diffusion only exerts strong damping when the scale shrinks to a small enough value. For example, a low Re case has strong diffusion, but the damping becomes weak when the previous diffusion has sufficiently damped the sharp structure.

Letting the "vorticity-equivalent accumulated convergence" $-\Delta h$ be the average accumulated convergence within a radius of r_u, we have $\Delta h = \widetilde{\Delta h}/\alpha_r^2 = \widetilde{\Delta h}/2$. It corresponds to $r_u = 8\sqrt{2}$ km and $\Delta h = 4$ km for the reference test. Based on (11), the new convective intermittency parameter to be frequently used is:

$$\frac{\Delta h}{H} = \delta_0 \Delta t \frac{R^2}{r_u^2}, \tag{12}$$

The end state mean absolute vorticity within r_u is denoted as $[\omega_a]^{r_u}$, which is expressed in a circulation conservation formulation as:

$$[\omega_a]^{r_u} = \omega_{a,0}\left(1 - \frac{\Delta h}{H}\right). \tag{13}$$

b. Multiple convection

1) THE EVOLUTION OF THE AVERAGE VORTICITY

As a macroscopic constraint, the mean low-mid level relative vorticity of the MCS (defined as ω^+) is directly related to the low-mid level mean divergence δ_0 and damping effects, based on Gauss theorem (Raymond et al. 2007; Montgomery and Smith 2017). It does not depend on how noisy the deep convection is. As the vorticity gradient at the MCS boundary is small, horizontal diffusion is unimportant. Raymond et al. (2007) have used this property to establish their model of system-averaged vorticity which includes an interactive δ_0 and a quadratic drag that both increase with the mean vorticity.

When there is a fixed δ_0 and no drag, a large enough domain ($L \gg R$) yields:

$$\omega^+ \approx -f_0 \delta_0 t. \tag{14}$$

This is demonstrated in Fig. 2a. The large domain dilutes the compensating divergence, so the vorticity squashing and therefore the negative relative vorticity outside of the MCS is small. Thus, the relative vorticity transported into the MCS is close to zero - a key assumption to be used in our vorticity PDF model. In appendix C, we include Rayleigh drag into this problem, and consider a finite domain correction. The drag directly damps ω^+, and the negative relative vorticity transported into the MCS indirectly damps ω^+.

To understand the maximum wind, we still need to know how ω^+ is distributed within the MCS, which involves the dynamics of eddies.

2) The evolution of eddies

Now we analyze the time evolution of the SWE reference test which is shown in the upper row of Fig. 3. We use the nondimensional time $t' = -\delta_0 t$ and choose the $t'_a = 0.50$, $t'_b = 1.46$ and $t'_c = 2.98$ snapshots that represent three characteristic stages. We analyze the SWE first. Figure 3a shows the $t' = t'_a$ early stage where vorticity patches are so sparse that the coupling between old vortices and new updraft is uncommon. Figure 3b shows the $t' = t'_b$ middle stage where some vortices are lucky enough to receive multiple mass forcings and begin to interact with each other. The converging flow facilitates the merger process by reducing the vortices' spacing while conserving their absolute circulation. Figure 3c shows the $t' = t'_c$ late stage where the 17 m s^{-1} tropical storm strength is roughly reached (e.g. Fig. 2b). The strong vortices merge into a large major vortex, with the newly-formed vorticity patches being rapidly distorted into filaments and wrapped around the core. The decrease of vorticity with radius produces an effective beta effect which migrates the small vortices toward the center, and helps the major vortex axisymmetrize itself (e.g. Terwey and Montgomery 2008; O'Neill et al. 2016). The merger is accompanied by elongated vorticity filaments that are produced by the strain in the mutual advection, as has been discussed by McWilliams (1990) and Dritschel and Waugh (1992). Though those filaments gradually wrap onto the vortex core, they are susceptible to strong dissipation when they are thin enough for diffusion to work. Some low vorticity columns which lie between the filaments will also be wrapped inward and get mixed in the end. This reminds us of the finding by Fang and Zhang (2011) that most of the negative or weak vorticity patch is mixed with the large vorticity patch near the center of a major vortex, rather than being repelled out. The behavior beyond the tropical depression regime (maximum wind > 17 m s^{-1}) is of less interest, because our simple convective scheme no longer works.

We compare the SWE test (named Ref-SWE) with WTGE test (named Ref-WTGE), as well as a low Coriolis parameter WTGE test (named Low-WTGE) that changes Coriolis parameter to $1/10$ of the reference value ($-\delta_0/f_0 \times 10$). Their convective seeding history is set to be identical. Figure 2b shows that both Fr and $-h'/H$ in the SWE test are much smaller than 1 by $t' = 3$, so the WTG condition (5) is satisfied in the three snapshots. Figure 3 shows that the vorticity field difference between the Ref-SWE and Ref-WTGE is indeed small, even indiscernible at $t'_a = 0.50$ and $t'_b = 1.46$. As for the Low-WTGE, the inflow does push the vorticity patches toward the MCS center significantly, but the vorticity distribution is less axisymmetric and has no filaments due to the much weaker rotational flow and therefore vortex interaction.

The traditional way to study the role of eddies in vortex formation or intensification is to diagnose the radial transport of vorticity by eddies (Hendricks et al. 2004; Montgomery et al. 2006), or check the energy cascade direction (e.g. Vallis et al. 1997; Wang et al. 2018). We propose a way to partly circumvent the turbulent process. The above simulations show that the vorticity produced by convection will sooner or later organize into a quasi-axisymmetric major vortex whose vorticity roughly monotonically decreases with radius. The latter is in agreement with the aircraft observation of a tropical depression by Middlebrooke (1988). Thus, the vorticity PDF can be related to the vorticity structure of the major vortex. Even if the monotonic and axisymmetric state is not completely reached, the vorticity PDF still qualitatively tells how compact the vortex is, which determines its ability to survive in a straining environment, as well as an upper bound of the maximum wind which signifies intensity. Note that the radial vorticity is not monotonic for a mature hurricane where deep convection at the eyewall makes the vorticity there larger than the quiescent eye (Schubert et al. 1999).

The PDF of the nondimensional absolute vorticity $x' = \ln(\omega_a/f_0)$ inside MCS is defined as σ. The σ of the three tests (Ref-SWE, Ref-WTGE and Low-WTGE) is shown in Fig. 4. The PDF evolves from a purely low vorticity dominated state to a wide spectrum, with a tail extending to high vorticity region. It is not surprising that the PDF of Ref-SWE and Ref-WTGE collapse very well. However, the rough collapse of Ref-WTGE and Low-WTGE is intriguing, given their dramatically different flow field. This is explained in the next section with a simple vorticity PDF model. The small difference between the PDF of Ref-WTGE and Low-WTGE will be attributed to eddy mixing in section 6a.

It is worth making a comparison with 3D turbulence cascade, where repetitive vortex stretching is also an important mechanism of scale reduction and vorticity amplification (Lundgren 1982; Tennekes and Lumley 2018). The main difference in this model is the constraint of vortex orientation by the 2D domain (the stratified atmosphere) and the purely random prescription of the stretching (updraft) position. These make a statistical theory possible.

5. A statistical theory of vorticity PDF

a. Motivation

Within this setup, the vorticity PDF is largely governed by a random vorticity stretching process under the influence of Rayleigh drag and eddy mixing. Thanks to the validity of WTG approximation, potential vorticity reduces to absolute vorticity, so we do not need to consider the area change of vorticity patches during adiabatic motion. The negative vorticity produced by the inertially-trapped compensating divergence near an updraft is also negligible. The eddy mixing, which does influence PDF via air column interactions, is a complicated process that is not included in this preliminary investigation.

In section 5b, we model the PDF of the random stretching process as a discrete Markov chain. In section 5c, it is updated to a hybrid discrete-continuous PDF problem that includes drag.

b. The random stretching problem

The vorticity production in one convective event obeys (13). For multiple convective events, a new updraft may hit an existing vorticity patch and concentrate the vorticity there through stretching. As the strength of each updraft is fixed, the vorticity evolves by migrating on a set of quantum vorticity levels in power law:

$$\omega_{a,m} = \omega_{a,0}\left(1 - \frac{\Delta h}{H}\right)^m,\ m = 0,\ 1,\ 2,\ \ldots; \omega_{a,0} = f_0. \tag{15}$$

This concept is illustrated in Fig. 5. The parameter $-\delta_0\widetilde{\tau_u}$ does not appear because it does not influence the end state of geostrophic adjustment, and the interaction between updraft is neglected due to $\sigma_u \ll 1$. Because the domain is much larger than the MCS, the descent is weak, so the negative vorticity production in the MCS due to vorticity squashing is neglected. As a new convection is seeded every Δt time interval, the time level is also discrete:

$$t_n = n\Delta t,\ n = 0,\ 1,\ 2,\ \ldots \tag{16}$$

Let $\sigma_{m,n}$ be the fractional area of $\omega_{a,m}$ at time level n. The quantity $\sigma_{m,n}$ can also be regarded as the discrete vorticity PDF which satisfies:

$$\sum_{m=0}^{\infty} \sigma_{m,n} = 1. \tag{17}$$

An updraft consumes the $\omega_{a,m-1}$ level area $\pi r_u^2(1-\Delta h/H)$, and the $\omega_{a,m}$ level gains area πr_u^2. Thus, the $\sigma_{m,n}$ evolution is essentially a discrete mapping of vorticity and time which is a linear

Markov chain:

$$\sigma_m^n = \sigma_m^{n-1}(1-p) + \sigma_{m-1}^{n-1}\frac{r_u^2}{R^2}\,, \quad m = 1,\ 2,\ \ldots, M-1;\ n = 1,\ 2,\ \ldots. \tag{18}$$

$$\text{with} \quad p \equiv \frac{r_u^2}{R^2}\left(1-\frac{\Delta h}{H}\right) < 1. \tag{19}$$

The p is the probability for an air column in the MCS to get involved in each updraft event. The term $\sigma_m^{n-1}(1-p)$ in (18) denotes the loss of m level vorticity due to the rise to $(m+1)$ level, and $\sigma_{m-1}^{n-1} r_u^2/R^2$ denotes the contribution from $(m-1)$ level. Note that the property $(1-p)+r_u^2/R^2 < 1$ indicates net mass loss in an updraft. Such loss is compensated by the inflow across the MCS boundary which has a flux that depends on δ_0 and is assumed to have zero relative vorticity due to the large domain effect. The lowest vorticity level σ_0^n is determined by both the inflow refreshment rate and the migration to σ_1^n level, with an initial value $\sigma_0^0 = 1$:

$$\sigma_0^n = (1-p)\sigma_0^{n-1} - \delta_0 \Delta t. \tag{20}$$

The solution of σ_0^n is:

$$\begin{aligned}\sigma_0^n &= (1-p)^n\left(1+\frac{\delta_0\Delta t}{p}\right) - \frac{\delta_0\Delta t}{p} \\ &= \left[1-\frac{r_u^2}{R^2}\left(1-\frac{\Delta h}{H}\right)\right]^{-\frac{t'}{(r_u^2/R^2)(\Delta h/H)}}\left(1+\frac{\Delta h/H}{1-\Delta h/H}\right) - \frac{\Delta h/H}{1-\Delta h/H}.\end{aligned} \tag{21}$$

Here we have used the nondimensional time $t' = -\delta_0 n\Delta t = -\delta_0 t$, and have used (12). For the reference value, $\delta_0\Delta t \approx -0.01$ and $p \approx 0.03$.

The change of σ_0^n with t' is shown in Fig. 6a. Three features are noted.

- The quantity r_u^2/R^2 has little influence on σ_0^n. Mathematically, it is due to the rough balance between the r_u^2/R^2 inside the middle bracket and the other one at the exponent.

- For small n (short time), $\sigma_0^n \approx (1-p)^n$, indicating that the compensating inflow is not important for early time when the MCS has not been occupied by vorticity patches.

- For $n \to \infty$ (long time), $\sigma_0^n \to -\delta_0 \Delta t/p = (-\Delta h/H)/(1-\Delta h/H)$, which is a constant that increases with the intermittency measure $-\Delta h/H$. An adjustment time scale τ_{σ_0} is obtained by linearizing $(1-p)^n$ to $1-np$ and finding its zero-crossing point $n = 1/p$. As a verification, we find that $(1-p)^{1/p}$ lies between 0.32 and 0.37 for $0 < p < 0.2$, which is quite robust. The expression of τ_{σ_0} is obtained with the help of (12) and (19): $\tau_{\sigma_0} = \Delta t/p = t/(np) = \delta_0^{-1}(\Delta h/H)/(1-\Delta h/H)$, which also increases with intermittency.

The solution of this discrete system is derived by analyzing the probability for a column to experience m convective events by $t = n\Delta t$ time, which turns out to be a weighted binomial distribution:

$$\sigma_m^n = \left[\begin{pmatrix} n \\ m \end{pmatrix} p^m (1-p)^{n-m} + \sum_{k=1}^{n-m} \begin{pmatrix} n-k \\ m \end{pmatrix} p^m (1-p)^{(n-k)-m} (-\delta_0 \Delta t) \right] \left(1 - \frac{\Delta h}{H}\right)^{-m},$$

$$\text{for} \quad n \geq m > 0, \quad \text{with} \quad \begin{pmatrix} n \\ m \end{pmatrix} = \frac{n!}{m!\,(n-m)!}. \tag{22}$$

It is easy to verify that (22) satisfies (18) and (21). As a comment, binomial and Poisson distributions have long been used to fit the probability of rare meteorological events (e.g. Thom 1957). Here σ_m^n is not only contributed to by columns originally inside the MCS, but also those from outside that come in later at $t = \Delta t,\ 2\Delta t,\ \ldots,\ (n-m)\Delta t$. For the native MCS columns, the probability to reach the m level within n updraft periods obeys a binomial distribution, as is shown in (22). Columns that come later at $t = k\Delta t$ time need to arrive at m level within $(n-k)\Delta t$ time, as is represented by each term in the summation. The binomial distribution demonstrates that to migrate to the same level m, newer columns must be luckier than older ones because they have fewer discrete opportunities. The nondimensional time interval $\Delta t' = -\delta_0 \Delta t$ is the rate of inflow refreshment brought by each updraft. To migrate to the m level, the columns need to shrink their area by $(1-\Delta h/H)^{-m}$. Thus, all sources of contribution to σ_m^n must be multiplied by this factor.

As p is very small ($p \approx 0.03$ for the reference test), the binomial distribution for large n (sufficient for $n \gtrsim 20$ or about $t' \gtrsim -\delta_0 \Delta t \times 20 \approx 0.2$ for the reference test) can be approximated as a Poisson distribution (Pishro-Nik 2014):

$$\begin{pmatrix} n \\ m \end{pmatrix} p^m (1-p)^{n-m} \approx \frac{(np)^m}{m!} e^{-np}. \tag{23}$$

As $np \sim t' \ll 10$ in the regime of interest, the Poisson distribution element cannot be further approximated as a normal distribution. Substituting (23) into (22), using $\delta_0 \Delta t = (\Delta h/H)(r_u^2/R^2)$, and rearranging to better manifest the contribution from the original MCS columns and newcomers, we get a simplification of (22):

$$\begin{aligned} \sigma_m^n &\approx \frac{(np)^m e^{-np}}{m!} \left(1 - \frac{\Delta h}{H}\right)^{-m} \left[1 + \sum_{k=1}^{n-m} \left(1 - \frac{k}{n}\right)^m e^{kp} \left(-\frac{\Delta h}{H} \frac{r_u^2}{R^2}\right)\right] \\ &\approx \frac{(np)^m e^{-np}}{m!} \left(1 - \frac{\Delta h}{H}\right)^{-m} \left[1 + t' \int_0^1 (1-s)^m e^{nps} ds\right]. \end{aligned} \tag{24}$$

Here the sum has been approximated as an integral. It is valid when $ds \approx 1/n = (r_u^2/R^2)(-\Delta h/H)/t'$ is small and $m \ll n$, therefore applicable to our $r_u/R \ll 1$ case at a not too small t'. Because the Poisson distribution parameter is $np = t'(1 - \Delta h/H)/(-\Delta h/H)$, the only physical parameter involved in this integral is $-\Delta h/H$. Why is r_u/R unimportant? Physically, for fixed δ_0 and $-\Delta h/H$, a wider updraft is equivalent to a bunch of narrower updrafts which are seeded at the same time and cannot not overlap with each other. It is this non-overlap requirement that causes the difference. However, the chance of overlap in seeding a bunch of narrower updrafts independently is already very small for $r_u/R \ll 1$, so the difference is tiny.

This analytical solution additionally tells how different ages of columns constitute a certain level of vorticity. This might be useful for studying tracer transport by a tropical depression. As σ_m^n is linked to the radial vorticity distribution of the major vortex at the later stage, (24) also qualitatively tells the age composition at different radial positions. Figure 7 shows the contribution to σ_m^n at $m = 2$ and $m = 5$ levels from the columns entering at $t_k = k\Delta t$ (only $k \geq 1$ is shown), with the reference test parameter. This fraction $\mu_m(k,n)$ is:

$$\mu_m(k,n) \equiv \left(1-\frac{k}{n}\right)^m e^{kp}\left(-\frac{\Delta h}{H}\frac{r_u^2}{R^2}\right)\left[1+\sum_{k=1}^{n-m}\left(1-\frac{k}{n}\right)^m e^{kp}\left(-\frac{\Delta h}{H}\frac{r_u^2}{R^2}\right)\right]^{-1}. \tag{25}$$

A "maximum-contribution age" always exists for a large n, because many older air columns have migrated to higher levels and the younger air columns do not have much chance to reach that level. This age is younger for a lower m, which is easier to reach.

c. The hybrid discrete-continuous PDF

The "vorticity-equivalent top hat" and therefore the discrete vorticity level system is only a mathematical approximation. Each updraft can produce a continuous range of ω_a, and the PDF increment at a certain ω_a can be contributed by a continuous range of ω_a below it. Meanwhile, the discrete base level $\omega_a = f_0$, which depends on the balance of convective occupation and inflow compensation, is well-defined. Thus, we propose a hybrid view that retains the $\omega_a = f_0$ level fractional area σ_0 as a discrete one, and let the larger ω_a be a continuous distribution σ_c.

As a standard technique, the original discrete vorticity levels can be viewed as a discrete sampling, or a finite-difference approximation to a continuous PDF (Pope 2001). Because the original discrete set of levels is a power law that is uniform on a logarithmic coordinate, we introduce the continuous levels as $x' = \ln(\omega_a/f_0)$, which has been used in Fig. 4. In comparison, the original discrete level is located at $x'_m = \ln(\omega_{a,m}/f_0) = m$, with an interval of $\Delta x' = \ln(1-\Delta h/H)$. We then introduce the continuous PDF σ_c, which approximately represents the homogenization of σ_m^n within $x'_m \pm (1/2)\Delta x'$:

$$\sigma_c\left(x'_m, t'\right) \approx \frac{\sigma_m^n}{\Delta x'}, \quad m = 1, 2, 3.... \tag{26}$$

The governing equation of σ_c, also called Kramers-Moyal equation (Pope 2001), is derived in the supplemental material.

The hybrid PDF is not only more physically realistic, but also straightforward to incorporate Rayleigh drag. It is hard to add drag to the Markov chain model, because the vorticity levels change continuously due to the drag. As a result, new vorticity levels are produced every Δt and the number of levels blows up.

The PDF of the discrete part, σ_0, is an updated version of (21). After replacing n by $t'/\Delta t'$ ($t' = -\delta_0 t$ and $\Delta t' = -\delta_0 \Delta t$) to make it continuous in time, we get:

$$\sigma_0(t') = (1-p)^{t'/\Delta t'}\left(1-\frac{\Delta t'}{p}\right)+\frac{\Delta t'}{p}. \tag{27}$$

How do the discrete and continuous part match with each other? In view of finite-difference, the discrete "grid cell" spans $0 \pm \Delta x'/2$. The domain of continuous PDF is heuristically set as $x' \in (\Delta x'/2, +\infty)$. Inspired by Sukhatme and Young (2011) in treating the vapor PDF equation of an advection-condensation model, the σ in this domain is set to satisfy the normalization condition: $\int_{\Delta x'/2}^{\infty} \sigma_c dx' = 1 - \sigma_0(t')$ which corresponds to a flux boundary condition at the left end $x' = \Delta x'/2$, as is derived in the supplemental material.

The deterministic problem of the continuous part σ_c which uses the nondimensional time $t' = -\delta_0 t$ is:

$$\frac{\partial \sigma_c}{\partial t'} + \frac{\partial F}{\partial x'} = -\sigma_c, \tag{28}$$

$$\text{with} \quad F = -D_1\sigma_c - \sum_{i=1}^{3} D_{i+1}\frac{\partial^i \sigma_c}{\partial x'^i} + \frac{\sigma_c}{\delta_0 \tau_d}(1-e^{-x'}), \quad x' \in (\Delta x'/2, +\infty), \tag{29}$$

$$F_0 \equiv F|_{x'=\Delta x'/2} = -\frac{d\sigma_0}{dt'} + (1-\sigma_0), \quad \sigma_c|_{x'\to\infty} = 0, \qquad \sigma_c|_{t'=0} = 0. \tag{30}$$

Here F is the probability current, and F_0 is the F at $x' = \Delta x'/2$. The vorticity migration process is part of F. The derivative terms come from a Taylor expansion that represents the nonlocal migration nature of the Markov chain. The drift, diffusion, dispersion, and hyper-diffusion coefficients are:

$$D_i = \frac{(-1)^{i-1}}{i!}\frac{H}{\Delta h}\left[\ln\left(1-\frac{\Delta h}{H}\right)\right]^i, i = 1,2,3,4. \tag{31}$$

Here $D_1 < 0, D_2 > 0, D_3 < 0, D_4 > 0$. F can include higher derivative terms, but we found that truncation to the D_4 term yields sufficient accuracy for our $-\Delta h/H \sim O(1)$. The full PDF expression is:

$$\sigma(x',t') = \sigma_0(t')\Theta(x') + \sigma_c(x',t'), \tag{32}$$

where Θ denotes Dirac-Delta function. Equations (27), (28), (30), (31) and (32) form a closed problem that can only be solved numerically in general.

Of the six nondimensional parameters that control the whole WTGE problem, the PDF problem is only controlled by two: $\Delta h/H$ on convective intermittency and $\delta_0\tau_d$ on drag. The updraft size r_u^2/R^2 does exist in the expression of $\sigma_0(t')$ but has tiny influence, as explained in section 5b. Physically, the $\widetilde{\tau_u}$ does not appear because it does not directly influence the end state of the vorticity spin up by an individual convection. The nondimensional independent variables show that the solution is self-similar to f_0 and δ_0. A larger f_0 (hurricane formation at higher latitude) systematically raises the magnitude of vorticity. A larger δ_0 magnitude (larger total MCS updraft mass flux) simply accelerates the PDF evolution. In fact, the problem can be extended to an unsteady $\delta_0(t)$ by replacing the temporal coordinate $t' = -\delta_0 t$ with a stretched one: $t' = -\int_0^t \delta_0(t'')\,dt''$, which is the accumulated convergence of the system (MCS). This is used in section 7 where the theory is applied to interpret the full physics three dimensional simulation. For the Markov chain model in section 5b where Rayleigh drag is not included, the only change is regarding Δt as a function of t in $t_n = n\Delta t$.

The "σ_c" term on the RHS of (28) is a linear damping factor that denotes the area shrinking due to flow convergence. The magnitude of the drift coefficient $|D_1|$ decreases with increasing

$-\Delta h/H$, but the magnitude of the higher order coefficients increases with $-\Delta h/H$, as is shown in Fig. 6c. This leads to a flatter tail on the PDF. It indicates that a more intermittent convective mode leads to smaller but stronger vorticity patches. The Rayleigh drag is essentially an "anti-advection" that pushes the PDF toward low vorticity region and accumulates there. It is only significant for a long enough time: $t' \gtrsim -\delta_0 \tau_d$.

Figure 6a and b shows the time evolution of σ_0 and F_0 for different $-\Delta h/H$. The F_0 is largest at the beginning, because every updraft can turn a piece of the vast $\omega_a = f_0$ region into $\omega_a > f_0$. It decreases rapidly to $1 - \sigma_0$ where the occupation by updraft is balanced by the supply of $\omega_a = f_0$ area by inflow. The adjustment time scale of F_0 is τ_{σ_0}, which is identical to that of σ_0. The less intermittent the updraft is, the larger F_0 is at the early stage due to the rapid occupation, and the faster F_0 falls back to 1.

d. The analytical solution in the uniform updraft limit

For $-\Delta h/H \to 0$ (very weak but frequent convection), the hybrid PDF problem renders an analytical solution. Here, $D_1 \to -1$, D_2, D_3, D_4 vanish, and F_0 contains a pulse at the beginning. The quantity σ_0 drops to 0 very fast due the rapid occupation by convection. Thus, the discrete part of the PDF occupies an infinitesimal space on x', and the hybrid problem is solely controlled by the continuous part which spans $x' \in (0, +\infty)$. This situation is equivalent to a uniform mass sink in the MCS, and the MCS dynamics is just the larger scale version of the single updraft vorticity spin up process introduced in appendix B.

Thus, the geostrophic adjustment solution in physical space can serve as a benchmark for the PDF equation. Through the derivation in the supplemental material, we get:

$$\sigma(x',t') = \sigma_c(x',t') = \begin{cases} [\Theta(t')+1]e^{-x'}, & x' \le t', \\ 0, & x' > t'. \end{cases} \tag{33}$$

The PDF is not monotonic: it consists of a $x' = t'$ peak followed by an exponentially decaying slope, without a high vorticity "tail" (e.g. Fig. 8a). The delta function part in PDF corresponds to the solid body vortex core. It consists of the columns initially inside the MCS. Now, we link the vorticity PDF with its physical distribution. The vorticity is rearranged, with the lowest vorticity at the rim of the MCS and the highest vorticity at its core. Each infinitesimally thin ring in physical space corresponds to an infinitesimally small bin in the PDF:

$$\int_0^r \frac{2\pi r}{\pi R^2} dr = \int_{x'}^{+\infty} \sigma dx'. \tag{34}$$

This recovers the physical space solution that consists of a solid body rotation core and a decaying skirt:

$$\omega_a = \begin{cases} f_0 e^{t'}, & \frac{r}{R} < e^{-t'/2} \\ f_0 \left(\frac{r}{R}\right)^{-2}, & \frac{r}{R} \ge e^{-t'/2} \end{cases}. \tag{35}$$

This is equivalent to (B1), after replacing $\widetilde{r_u}$ by R, $-\delta_u \widetilde{T_u}$ by $t' = -\delta_0 t$ and $\omega_{a,0}$ by f_0. Let $r_b = Re^{-t'/2}$ be the radius of the solid body rotation core. The finite domain effect reduces the peak vorticity in the numerical solution and the diffusion smears the vortex core rim, but the theory is otherwise very similar (Fig. 8b,c).

The tangential velocity V_θ is obtained by integrating (35) radially. Upon being rescaled by $f_0 R$, it is viewed as a local Rossby number:

$$\frac{V_\theta}{f_0 R} = \begin{cases} (e^{t'}-1)\frac{r}{2R}, & \frac{r}{R} < e^{-t'/2}, \\ \frac{1}{2}\left(\frac{r}{R}\right)^{-1}(1+t') + \left(\frac{r}{R}\right)^{-1}\ln\left(\frac{r}{R}\right) - \frac{r}{2R}, & 1 \geq \frac{r}{R} \geq e^{-t'/2}, \\ \frac{t'}{2}\frac{R}{r}, & \frac{r}{R} > 1. \end{cases} \tag{36}$$

Equation (36) is also the result of column angular momentum conservation, which is approximately valid during the spin up of the lower free tropospheric flow. Unlike Rankine vortex whose radius of maximum azimuthal mean wind is located at the boundary of its solid body core, that of this model (defined as $r = r_m$) is located outside of the solid body core $r = r_b$, and the maximum azimuthal mean wind $\overline{V_m}$ is always a bit larger than the core boundary velocity V_b (e.g. Fig. 8b,c). Though r_m and $\overline{V_m}$ do not have analytical expression, r_b and V_b do:

$$\frac{V_b}{f_0 R} = \sinh\left(\frac{t'}{2}\right) \quad \text{at} \quad r_b/R = e^{-t'/2}. \tag{37}$$

A Taylor expansion of V_θ around r_b shows that $r_m \approx r_b[1+(1-e^{-t'})/4] > r_b$, and $\overline{V_m} > V_b$. In section 6c, we will show that V_b is a good approximation of $\overline{V_m}$ and is useful for understanding the evolution of maximum wind.

6. Validation and sensitivity tests

In this section, we compare the PDF theory with WTGE numerical simulation, and discuss how the convective parameters influence the compactness and intensity of the idealized tropical depression. We primarily perform six tests:

- EXP-a, the reference test (the Ref-WTGE).
- EXP-b: the $-\widetilde{\Delta h}/H \times 1/8$ test. It is performed by making the convective lifetime $-\delta_0 \widetilde{T_u}$ be 1/8 of the reference value, to hold the nondimensional updraft mass sink rate $\widetilde{Q_m}/(-\delta_0 H) =$

$(\widetilde{\Delta h}/H)/(-\delta_0 \widetilde{T_u})$. We will see $-\delta_0 \widetilde{T_u}$ is not a sensitive parameter, so letting it change together with $-\widetilde{\Delta h}/H$ should not add meaningful complexity.

- EXP-c: the τ_d drag test, with $-\delta_0 \tau_d = 2.0$, equivalent to a damping time scale of $\tau_d \approx 2$ days. A realistic τ_d based on the estimation of Montgomery et al. (2001) for a weak hurricane is ~ 3 days. We use this exaggeratedly short τ_d to theoretically understand the influence of strong drag, and to test the PDF model as well.

- EXP-d: the $\widetilde{r_u}/R \times 2$ test, performed by making $\widetilde{r_u} \times 2$. With the nondimensional argument in appendix A, it can also be regarded as halving the MCS radius.

- EXP-e: the $-\delta_0 \widetilde{T_u} \times 1/4$ test, performed by making updraft mass sink rate $\widetilde{Q_m} \times 4$.

- EXP-f: the $\mathrm{Re} \times 1/2$ test, performed by doubling ν.

These, together with the $-\delta_0/f_0 \times 10$ test (Low-WTGE) introduced in section 4b2), cover all the six nondimensional parameters.

a. Vorticity PDF

Figure 9 shows the PDF predicted by the analytical solution of the Markov chain in (24) and the numerical solution of the continuous part of the hybrid theory (σ_c) against the WTGE simulation, at $t'_b = 1.46$ and $t'_c = 2.98$ (the middle and late stage). First, the agreement with the hybrid PDF theory and the Markov chain is good, except for the τ_d test where the discrete PDF is unavailable. Second, the agreement of the hybrid PDF theory with the simulation is good, except that there is overestimation at the large x' region and underestimation at the middle x' region (a bump). Such deviation is more significant for $t'_c = 2.98$ than $t'_b = 1.46$, and is weaker for the τ_d test.

We judge that turbulent mixing is responsible for a substantial portion of the deviation, because the $-\delta_0/f_0 \times 10$ test has weaker turbulent mixing and is closer to the theory (Fig. 4). The eddies not only help concentrate positive vorticity at the core, but also mix the low and high vorticity columns into the middle range. The mixing looks like an "anti-diffusion" on PDF (Pope 2001). This also explains why the τ_d test has a lower deviation: the turbulence is damped by drag and therefore cannot produce small-scale filaments effectively.

Only the PDF of the $-\Delta h/H$ and τ_d tests are significantly different from the reference test. This agrees with the theoretical prediction that the PDF problem is only controlled by $-\Delta h/H$ and $-\delta_0\tau_d$ to the lowest order. The vorticity PDF is less spread when $-\Delta h/H$ is small. The τ_d test shows that Rayleigh drag damps both middle and high vorticity significantly. The PDF is related to the spatial structure of the major vortex (Fig. 10). A major vortex has been established, though some asymmetric structure still exists due to the unfinished merger process. In the $-\Delta h/H \times 1/8$ test, the major vortex is axisymmetric but less compact. In the τ_d test, the major vortex is small and weak compared to its filaments due to the weaker vorticity magnitude and therefore weaker vortex interaction.

There is some dispersion of the PDF ensemble, especially at the large vorticity range where some bins are empty but some are not. Such uncertainty is due to the spatio-temporal discrete nature of convective events. The $-\Delta h/H = -\delta_0\tau_{rev} \to 0$ case converges to fully deterministic due to the infinitely short convective revisit time.

The PDF is insensitive to viscosity for the Re range we use. This is due to the two main dissipation processes in our model: the flattening of a vortex patch by diffusion after a stretching event, and the eddy mixing, are all small scale processes that are sufficiently separated from the scale of vortex interaction. The outcome of dissipation is important, but the Re-dependent dissipative scale is unimportant to this problem.

b. Asymmetry and monotonicity

The relationship between the PDF and radial vorticity distribution is closer when the vorticity is more axisymmetric and more radially monotonic. We define a "non-axisymmetric and non-monotonic index" (NAMI) to quantify these two factors. The vortex center is defined as the maximum point of a Gaussian filtered vorticity field (with a filter length scale of $0.3R$). This treatment loosely considers both the geometrical center and the strongest eddy's center. A larger filter length adds weight to the former. Based on this, we define the radial profile of the azimuthal-average vorticity as $\overline{\varpi}$. We then define $\overline{\varpi_p}$ as the axisymmetric and monotonic vorticity field obtained from re-sorting all the vorticity grid points in a circle with a radius of R whose center is the vortex center. The column (grid point) with the highest vorticity is put in the center and the lower vorticity columns are wrapped around it. The NAMI is defined as a normalized quadratic difference between $\overline{\varpi}$ and $\overline{\varpi_p}$:

$$\mathrm{NAMI} \equiv \frac{\int_0^1 (\overline{\varpi} - \overline{\varpi_p})^2 \, d(r/R)}{\int_0^1 \overline{\varpi}^2 d(r/R)}, \tag{38}$$

where r denotes the distance from the vortex center. To give more weight to the central region, the integral in (38) is not weighted by r. The NAMI is zero when the vortex is perfectly axisymmetric and monotonic. The procedure is analogous to calculating the available potential energy of a stratified flow (Vallis 2017). Apparently, a higher $-\delta_0/f_0$ yields a lower NAMI due to the lack of eddies that could axisymmetrize the flow (e.g. Fig. 3g-i where the $-\delta_0/f_0 \times 10$ test is presented).

In all sensitivity tests except for the τ_d test, the NAMI decreases quasi-linearly with time toward zero by $t' = 3$, but it never reaches zero due to the ceaseless convection that produces asymmetry and non-monotonicity (Fig. 11). The τ_d case decreases much more slowly due to the damped vortex interaction. The $-\widetilde{\Delta h}/H \times 1/8$ test yields a much lower NAMI than the reference test, due to the more fine-grained, and therefore more homogeneous and axisymmetric forcing. Its standard deviation is the smallest among all, because the limit of a fine-grained mode is the full determinacy. The $\widetilde{r_u}/R \times 2$ test also yields a low NAMI. In this case, a wider updraft spins up a wider initial vortex, and the convective frequency is also smaller (for a fixed δ_0). As a result, the length scale of forcing is larger, and the system requires fewer merger events to form a major vortex. This explains why its NAMI is already small at the beginning. If we interpret the $\widetilde{r_u}/R \times 2$ test as halving R, we can say that for a fixed δ_0 (convective vigor), a smaller MCS leads to faster axisymmetrization of the vortex. Kilroy and Smith (2017) also reported faster axisymmetrization for a smaller initial middle level vortex (roughly equivalent to our R) in their 3D cloud-resolving simulation. However, their initial mid level vortex's vorticity is set to be larger for a larger vortex, and they interpreted the faster axisymmetrization as the higher convective vigor caused by the higher boundary layer top pumping velocity which is driven by the stronger initial vortex. The NAMI is smaller for a higher viscosity (Re $\times 1/2$), due to the stronger damping on the filaments. The convective duration time $-\delta_0\widetilde{T_u}$ has little influence on NAMI for the parameters we study.

c. *Intensity*

What determines the maximum wind (intensity) of a vortex? First, the circulation theorem tells that a more compact vortex should have a larger maximum wind. A more compact vortex also has a higher inertial stability, as well as a higher survivability in a strain field (Dritschel 1990). A point vortex, whose vorticity is concentrated in an infinitesimal core, is the most robust one with an infinite maximum wind. Second, a lower NAMI enhances the maximum wind: a circular vorticity patch yields the highest peripheral velocity due to its minimized perimeter. As a higher $-\Delta h/H$ leads to higher compactness and higher NAMI at the same time, which factor dominates?

As the compactness is related to the convective intermittency, the least compact vortex is the uniform forcing case ($-\Delta h/H \to 0$) discussed in section 5d. We now use the expression of V_b and

r_b in (37) to understand the maximum azimuthal mean azimuthal wind $\overline{V_m}$ and its radius r_m in the simulation. The V_b rises with time and r_b contracts with time. The V_b consists of a linear regime at $-\delta_0 t \lesssim 1$ where $V_b/(f_0 R) \approx -\delta_0 t/2$, and an exponential regime at $-\delta_0 t \gtrsim 1$ where $V_b \propto e^{-\delta_0 t/2}$. The growth is dominated by the stretching of a constant planetary vorticity in the first regime and the stretching of a growing relative vorticity in the second regime. The V_b and r_b provide a theoretical reference for the magnitude of $\overline{V_m}$ and r_m for the finite $-\widetilde{\Delta h}/H$ cases.

Figure 12a shows that the maximum total wind V_{max} increases with $-\widetilde{\Delta h}/H \to 0$. Thus, the vorticity compactness dominates the asymmetry in determining the intensity. The $\widetilde{r_u}/R \times 2$ test has a larger V_{max} than the reference test at the early stage, in accordance with its lower NAMI at the early stage. In all tests, the initial jump of V_{max} for the finite $-\widetilde{\Delta h}/H$ tests is due to the convergent flow of updrafts. At the later stage where the convergent flow is far smaller than the rotational flow, all the V_{max} grows quasi-exponentially at a rate of $-\delta_0/2$, similar to V_b.

Figure 12b and c show the dependence of V_{max}, $\overline{V_m}$ and r_m on $-\widetilde{\Delta h}/H$ at $t'_c = 2.98$ by which time the major vortex has roughly formed. The expectation and standard deviation of both V_{max} and $\overline{V_m}$ increase significantly with $-\widetilde{\Delta h}/H$. The expectation of r_m drops with increasing $-\widetilde{\Delta h}/H$, featuring a more compact vortex, as is visualized in Fig. 10. While the lower bound of the expectation of V_{max} is provided by the $-\widetilde{\Delta h}/H \to 0$ case, the upper bound is provided by enforcing a NAMI $\to 0$ state for the theoretical PDF of a given $-\widetilde{\Delta h}/H$. The azimuthal velocity $V_U(r)$ of such a reconstructed vortex is transformed from the vorticity PDF using the differential form of (34):

$$\begin{aligned}\frac{V_U(r)}{f_0 R} &= \frac{1}{f_0 R}\frac{1}{r}\int_0^r \overline{\omega_p}(r')r'dr' \\ &= \frac{R}{2r}\int_{x'}^{+\infty} \sigma(x'',t')(e^{x''}-1)dx''.\end{aligned} \tag{39}$$

As the integral requires σ value at the high x' range, we use the interpolated discrete PDF analytical solution (24), which is computationally more accurate and cheaper than the numerical solution of the continuous PDF equation (28). The maximum V_U on the radial profile, $V_{Um} \equiv \max\{V_U\}$, is the theoretical upper bound. It increases with $-\widetilde{\Delta h}/H$ (Fig. 12b). The corresponding radius r_{Um}, which is a lower bound of r_m, decreases with $-\widetilde{\Delta h}/H$ (Fig. 12c). They encapsulate most of the WTGE result. In another view, this reconstructed vortex is driven by an equivalent axisymmetric convergence which is redistributed from the PDF of convergence (a pure Poisson distribution). A larger $-\widetilde{\Delta h}/H$ leads to a more compact convergence, and therefore a more compact vortex.

The ratio V_{Um}/V_b can be regarded as an "acceleration potential" of the mean flow by the eddies. The ratio V_{max}/V_{Um} can be regarded as an "acceleration efficiency", which is always below unity due to the asymmetry, non-monotonic vorticity profile and eddy mixing that prevent the theoretical maximum wind from being reached. The velocity upper bound V_{Um} is different from the equilibrium maximum intensity of Emanuel (1986) in that it only applies to the growing process and neglects damping. It is also not fully closed because it only tells the growth rate with respect to $t' = -\delta_0 t$, rather than t.

In a word, more intermittent convection generally makes the tropical depression more intense. The higher fluctuation on vorticity PDF and vorticity spatial distribution (higher NAMI) make the intensity less deterministic.

7. Comparison with a cloud-permitting simulation

To validate the hypothesis of the vorticity Markov chain, we run a cloud-permitting simulation of rotating radiative convective equilibrium (RCE) problem with the Bryan Cloud Model (CM1, Bryan and Fritsch 2002). The domain size is 1080^2 km^2, with doubly-periodic boundary condition and a uniform sea surface temperature. The physical process is mostly identical to the full-physics "configured RCE test" in CM1. It uses Morrison double-moment microphysics scheme (Morrison et al. 2005), RRTMG radiation scheme, and the simple planetary boundary layer scheme by Bryan and Rotunno (2009). The only difference is the surface model where we choose "sfcmodel=3", the revised scheme for WRF model. It provides a more realistic (higher) surface flux in RCE simulation than the default "sfcmodel=1".

This is a spontaneous tropical cyclogenesis problem without a prescribed initial vortex. This setup is clean and easy to implement, but the relevance to the real atmosphere which is full of disturbances and large-scale forcing is still in doubt (e.g. Dunkerton et al. 2009). We follow Wing et al. (2016) to set the SST as 305 K, which is higher than the climatology but avoids a much larger domain which is required to spin up a tropical cyclone with a normal SST. The grid interval is 2 km, which roughly permits the existence of deep convection. The Coriolis parameter is a constant value of $f_0 = 10^{-4}$ s^{-1}. The motivation for using such a high f_0 is to make the generated tropical cyclone small enough to fit the domain (Khairoutdinov and Emanuel 2013; Muller and Romps 2018). The initial sounding of potential temperature and vapor mixing ratio uses the horizontally-averaged profile of a 120^2 km^2 small-domain simulation with identical parameter setting run to the end of day 59, by which time an equilibrium state has approximately established.

A convective cluster evolves out of the seemingly random convection by day 32. It evolves to a ~ 20 m s^{-1} tropical storm stage ((AMS-Glossary 2012)) by day 36, and then reaches a peak maximum surface wind around 70 m s^{-1} by day 42, as is shown in Fig. 13a. Figure 14 shows the 1.18-6.25 km averaged vertical vorticity (regarded as the low-mid level) by $t_A = 31.21$ days, $t_B = 34.12$ days and $t_C = 37.04$ days, which correspond roughly to the MCS formation time, a sample of vortex development time and the peak time of the low-mid level convergence. Two reasons may contribute to the production of negative vorticity: the vorticity dipoles due to the tilting of horizontal vorticity (vertical shear) to the vertical by either updraft or downdraft (Kilroy et al.

2014), as well as the subsiding shell around the updraft which is driven by the evaporative cooling of hydrometeors or simply the nonhydrostatic compensating subsidence (Smith and Nicholls 2019). The vertical shear is part of the system circulation, which is omitted in our single layer model. To further study the vorticity PDF, we need to define the MCS region and calculate the low-mid level convergence.

We set the MCS size to be $R = 250$ km based on visual inspection of the vigorous convective region, as is indicated by the white circle in Fig. 14. The system (MCS) center is set as the maximum 30-km Gaussian filtered low-mid level vertical vorticity. The low-mid level refers to the vertical average between 1.18-6.25 km. No density weighting is used in calculating the vertical average of vertical vorticity. The vertical structure of the filtered vertical vorticity at the vortex center is positive below 10 km and weakly negative between 10 and 15 km (Fig. 13b). At t_A, the vorticity attains its maximum near 5 km height, and the maximum level decreases gradually toward the surface with time.

The δ_0 in our WTGE model means the convection-induced lower free tropospheric divergence. For the 3D simulation, δ_0 is calculated as the 1.18-6.25 km height averaged bulk divergence (without density weighting) within $R = 250$ km (Fig. 13c). It is only a coarse approximation to δ_0, because it also contains the Ekman pumping-induced divergence. Its magnitude increases to around $0.07 f_0$ by day 37 and then decreases. There is an oscillation with a period of ~ 0.5 day, which we speculate to be due to either the stationary gravity wave trapped in the doubly periodic domain, or the periodic burst of the precipitation-driven gustiness. The MCS-averaged rainfall rate, which represents column net latent heat release, increases between day 32 and 42 (Fig. 13c). The different trend of the convergence and rainfall indicates the weakening of free-tropospheric entrainment by the growing inertial stability (Kilroy et al. 2017). This, together with the earlier drop of the central region convective available potential energy (CAPE, Fig. 13a) indicate that our one-layer model gradually becomes invalid after the maximum $-\delta_0$ time. The characteristic $-\delta_0/f_0$ in its climbing phase is around 0.04. This is smaller than that used in our one-layer model which is suitable for the lower Coriolis parameter (4.99×10^{-5} s^{-1}).

The δ_0 is used to rescale the temporal coordinate: $t' = -\int_{t_A}^{t} \delta_0(t'')dt''$, whose relation to the real time t is shown in Fig. 15a. The initial $t' = 0$ time is chosen as t_A where the MCS is just discernible. The t_B and t_C correspond to $t'_B = 0.17$ and $t'_C = 0.86$. Fig. 15b shows the system-averaged (within the radius R) low-mid level vertical vorticity ω^+ roughly obeys $\omega^+/f_0 \approx t'$, though there is still $\omega^+/f_0 < t'$. The deviation could be due to the free-tropospheric dissipating effect such as cumulus drag, or the finite domain effect as is explored below. Starting from (C4), neglecting drag ($\tau_d \to \infty$) and assuming an unsteady $\delta_0(t)$, we get:

$$\frac{\omega^+}{f_0} = \frac{S^-}{S^+}\left(1 - e^{-\frac{S^+}{S^+ + S^-}t'}\right), \tag{40}$$

where $S^+ = \pi R^2$ is the area of the MCS and $S^- = L^2 - S^+$ is the rest of the area in the domain. This solution is much closer to the simulation result in Fig. 15b.

The low-mid level vertical vorticity PDF at the three snapshots are shown in Fig. 16. On the positive vorticity side, the high vorticity tail grows, and the slope flattens. This is qualitatively similar to the analytical solution of Markov chain in (24), which is calculated with an arbitrary $-\Delta h/H = 4/5$ (the reference value), $r_u = 8\sqrt{2}$ km and $R = 250$ km. The first difference is that the Markov chain seems to lag behind the evolution. This is because, before the low-mid level convergence starts, the vorticity already evolves to a distribution which is a rough balance between random stretching and damping. In the future, we will derive and use the balanced PDF to initialize the PDF model, rather than a quiescent state. The second difference is that the PDF value at the low vorticity end (around $x' = \ln(\omega_a/f_0) \sim 1$) is smaller. This loss could be due to the occupation by negative vorticity which does not exist in our PDF model. The negative vorticity also grows, which is probably also favored by the random stretching.

8. Discussion

This paper advances the understanding of vorticity structure of a tropical depression, which determines its intensity and ability to survive in a straining environment. In a shallow water equation model (SWE) that mimics the lower troposphere, we put random mass sinks in a circular region to mimic convection in a mesoscale convective system (MCS) which is the hurricane precursor. The numerical simulation shows that the vorticity produced by repetitive convective stretching is aggregated to a large major vortex via both merger and the converging flow, qualitatively capturing the vorticity evolution reported by previous 3D simulations. As such a vortex has a quasi-monotonic vorticity radial distribution, its structure is linked to a vorticity PDF, which is the theme of this paper.

First, we show that the SWE satisfies the weak temperature gradient approximation in a typical tropical depression genesis problem where Froude number Fr is small. This makes convective heating equivalent to convergence, and potential vorticity equivalent to absolute vorticity ω_a. Simulations show that the PDF depends mainly on random convective stretching and Rayleigh drag, and is modified by eddy mixing. When there is convective stretching alone, the PDF is approximately governed by a "Markov process" where air columns migrate on a set of quantum vorticity levels. Its analytical solution is a superposition of Poisson distributions weighted by the fraction of columns that enter the MCS at different times. Based on this, a better description that uses a hybrid PDF with the discrete base level $\omega_a = f_0$ and the continuous higher levels continuous is established.

As has been verified by the one-layer model simulation, the PDF problem is governed by two nondimensional parameters: the accumulated convergence in a convective event $-\Delta h/H$ which measures the convective intermittency, and the Rayleigh drag scaled by MCS mean divergence $-\delta_0\tau_d$. The problem is self-similar to Coriolis parameter f_0 which nondimensionalizes ω_a, and MCS mean divergence δ_0 which nondimensionalizes t. For fixed δ_0, a higher $-\Delta h/H$ represents a more coarse-grained convective mode that leads to a wider PDF with more high vorticity columns, as well as a higher uncertainty (lower predictability). A shorter drag time scale $-\delta_0\tau_d$ damps vorticity magnitude and delays the vorticity aggregation.

An intense major vortex not only requires a wide PDF which provides high vorticity columns to serve as a compact core, but also a more axisymmetric and monotonic vorticity spatial distribution. The newly introduced NAMI index (zero when fully axisymmetric and monotonic) drops significantly in a few system convergence time scales ($-\delta_0^{-1}$). The system is more axisymmetric when convection is less intermittent, the $-\delta_0/f_0$ is smaller which enhances the eddy merger, and the $\widetilde{r_u}/R$ is larger which makes the scale separation between an updraft and the major vortex smaller. The intensity is quantified by the maximum total wind V_{max}, which grows quasi-exponentially at a rate of $-\delta_0/2$ as the vortex spins up. Both the ensemble average and the standard deviation of V_{max} increase with $-\Delta h/H$. Thus, when convection is more intermittent, the expectation of vortex intensity is higher despite the stronger asymmetry, and its uncertainty is more significant. Note that the link of vorticity PDF with the monotonic vorticity structure and therefore wind distribution might be a privilege of the circular seeding (convective) geometry. If the seeding region is set as a band to simulate the Inter Tropical Convergence Zone, the structure will suffer from shear instability, and a PDF model is not enough to tell the wind distribution.

The theory is compared to a cloud-permitting simulation of spontaneous tropical cyclogenesis with CM1 model, using the rescaled time coordinate $t' = -\int \delta_0 dt$. The PDF of 1.18-6.25 km height vertically averaged vertical vorticity within a 250 km convective region also shows the growth of the high vorticity tail, and the positive vorticity side qualitatively agrees with our Markov chain analytical solution.

Many more things could be done for investigating tropical cyclogenesis with this one-layer model:

- The turbulent process is circumvented in the theory, but it is required for understanding both the time scale of axisymmetrization (drop rate of NAMI) and the estimate of eddy mixing effect on vorticity PDF. The latter is an important research topic in 2D non-divergent turbulence (e.g. Pasquero and Falkovich 2002).
- The convective scheme could be updated to consider the long-lived rotating convection which is identified in the simulation of Smith and Nicholls (2019). The interaction of moist convective vortices (Boubnov and Golitsyn 1986; Wang and Holland 1995; Schecter 2017), which is a deviation from a Markov process, should be considered.
- The model can be extended to consider more adverse factors that may prevent the MCS from developing into a hurricane. The survival ratio is important for hurricane climatology (Hsieh et al. 2020). Apart from the drag, negative vorticity production by downdrafts should be considered. Perhaps the horizontal shear and Rossby wave dispersion (on a beta plane) are most suitable to study, because they test the vortex's compactness which we judge to depend on convective intermittency.

An extension to at least two vertical layers is needed to address the complicated vorticity pattern produced by tilting (Kilroy et al. 2014), as well as the transition from a stratiform-dominated MCS with a middle level vortex to a convective-dominated state with a low-level vortex (Montgomery et al. 2006).

APPENDIX A

The nondimensional SWE and WTGE governing equation

Using $-\delta_0^{-1}$ as the time scale, R as the horizontal length scale, H as the vertical length scale, $-\delta_0 R$ as the horizontal velocity scale, and $-\delta_0 H$ as the vertical velocity scale, we introduce the nondimensional variables t^*, $\mathbf{x}^*$, h^*, ω_z^*, δ^*, $\mathbf{u}^*$, Q_u^*, Q_{rad}^*, ψ^* and ϕ^*, which obey:

$$t = t^*(-\delta_0^{-1}), \quad \mathbf{x} = \mathbf{x}^* R, \quad h = h^* H, \quad \omega_z = \omega_z^*(-\delta_0), \quad \delta = \delta^*(-\delta_0), \quad \mathbf{u} = \mathbf{u}^*(-\delta_0 R),$$
$$Q_u = Q_u^*(-\delta_0 H), \quad Q_{rad} = Q_{rad}^*(-\delta_0 H), \quad \psi = \psi^*(-\delta_0 R^2), \quad \phi = \phi^*(-\delta_0 R^2). \tag{A1}$$

The nondimensional gradient operator is $\nabla^* \equiv \mathbf{i}\partial/\partial x^* + \mathbf{j}\partial/\partial y^*$.

For SWE, we substitute (A1) into (1), (2), (8), and with the help of (10) to obtain:

$$\frac{\partial h^*}{\partial t^*} + \nabla^* \cdot (\mathbf{u}^* h^*) = Q_u^* + Q_{rad}^* + \frac{1}{\mathrm{Re}} \nabla^{*2} h^*, \tag{A2}$$

$$\frac{\partial \mathbf{u}^*}{\partial t^*} + \mathbf{u}^* \cdot \nabla \mathbf{u}^* + \left(\frac{-\delta_0}{f_0}\right)^{-1} \mathbf{k} \times \mathbf{u}^* = -\mathrm{Bu}^{-1} \left(\frac{-\delta_0}{f_0}\right)^{-2} \nabla^* h^* + \frac{\mathbf{u}^*}{\delta_0 \tau_d} + \frac{1}{\mathrm{Re}} \nabla^{*2} \mathbf{u}^*. \tag{A3}$$

$$Q_u^* + Q_{rad}^* = \sum_{n=1}^{+\infty} Q_n^*(\mathbf{x}^*, t^*) + \frac{\pi R^2}{L^2}, \quad \text{with} \quad Q_n^*(\mathbf{x}^*, t^*) = \widetilde{Q_m}^* e^{-\frac{|t^* + \delta_0 t_n|^2}{\delta_0^2 \widetilde{\tau_u}^2} - \frac{|\mathbf{x}^* - \mathbf{x_n}/\mathbf{R}|^2}{(\widetilde{r_u}/R)^2}}. \tag{A4}$$

$$\widetilde{Q_m}^* = \frac{\widetilde{Q_m}}{-\delta_0 H} = -\frac{R^2}{\widetilde{r_u}^2} \frac{\Delta t}{\widetilde{T_u}} = -\frac{\widetilde{\Delta h}}{H} \frac{1}{\delta_0 \widetilde{T_u}}. \tag{A5}$$

For WTGE, we substitute (A1) into (3), (6) and (7) to get:

$$\frac{\partial \omega^*}{\partial t^*} + \mathbf{u}^* \cdot \nabla^* \omega^* = -\delta^* \left(\omega^* - \frac{f_0}{\delta_0}\right) + \frac{\omega^*}{\delta_0 \tau_d} + \frac{1}{\mathrm{Re}} \nabla^{*2} \omega^*. \tag{A6}$$

$$\mathbf{u}^* = \mathbf{k} \times \nabla^* \psi^* + \nabla^* \phi^*, \quad \text{with} \quad \nabla^{*2} \psi^* = \omega^*, \ \nabla^{*2} \phi^* = \delta^*. \tag{A7}$$

$$\delta^*(\mathbf{x}^*, t^*) = \sum_{n=1}^{+\infty} \delta_{u,n}^*(\mathbf{x}^*, t^*) + \frac{\pi R^2}{L^2}, \quad \text{with} \quad \delta_{u,n}^*(\mathbf{x}^*, t^*) = \delta_{um}^* e^{-\frac{|t^* + \delta_0 t_n|^2}{\delta_0^2 \widetilde{\tau_u}^2} - \frac{|\mathbf{x}^* - \mathbf{x_n}/\mathbf{R}|^2}{(\widetilde{r_u}/R)^2}}. \tag{A8}$$

$$\delta_{um}^* = \frac{\widetilde{Q_m}}{-\delta_0 H} = -\frac{\widetilde{\Delta h}}{H} \frac{1}{\delta_0 \widetilde{T_u}}. \tag{A9}$$

The above equations show that there are six nondimensional parameters for WTGE: $-\delta_0/f_0$, $-\widetilde{\Delta h}/H$, $-\delta_0\widetilde{T_u}$, $\widetilde{r_u}/R$, $-\delta_0\tau_d$ and Reynolds number $\mathrm{Re} = f_0R^2/\nu$. For SWE, there is an additional $\mathrm{Bu} = R^2/L_R^2 = (f_0R)^2/c_0^2$ which accounts for the deviation from weak temperature gradient.

APPENDIX B

The vorticity production in a single updraft and the subsequent viscous damping

1) The updraft stage

Supposing the background is a (locally) solid body rotating flow with absolute vorticity $\omega_a = \omega_{a,0}$. A convergence at a constant value of $-\delta_u$ is suddenly imposed to a circular region with a radius of $\widetilde{r_u}$ for $\widetilde{T_u}$ time. Such a top-hat convergence is a qualitative representation of the Gaussian profile used in the simulation. We assume that horizontal diffusion and drag are unimportant in such a short time. At $t = \widetilde{T_u}$, angular momentum conservation yields:

$$\omega_a = \begin{cases} \omega_{a,0}e^{-\delta_u\widetilde{T_u}}, & \frac{r}{\widetilde{r_u}} < e^{\delta_u\widetilde{T_u}/2}, \\ \omega_{a,0}\left(\frac{r}{\widetilde{r_u}}\right)^{-2}, & \frac{r}{\widetilde{r_u}} \geq e^{\delta_u\widetilde{T_u}/2}. \end{cases} \tag{B1}$$

Note that a steady state vorticity with a positive circular divergence forcing (balanced by Rayleigh drag) has been approximately solved by Sobel et al. (2001) to demonstrate their WTG framework.

Air columns that are initially within $\widetilde{r_u}$ form a solid body rotation core. The outer region consists of columns entrained into the convection, so they are stretched less. The role of convection is concentrating vorticity, with the maximum absolute vorticity rising to $\omega_{a,0}e^{-\delta_u\widetilde{T_u}}$, and the length scale shrinking from $\widetilde{r_u}$ to $\widetilde{r_u}e^{\delta_u\widetilde{T_u}/2}$ where $\delta_u\widetilde{T_u} = \widetilde{\Delta h}/H$. The accumulated convergence $-\widetilde{\Delta h}/H$ can be understood as an area shrinking ratio.

2) THE POST-UPDRAFT STAGE

After the convection, the vorticity patch is susceptible to diffusion which will change its shape before the next convection hits it. The diffusion time scale τ_{diff} is estimated with ν and the vorticity patch length scale $l_{diff} = \widetilde{r_u} e^{\delta_u \widetilde{T_u}/2}$. Now we apply these results to a Gaussian-shape convergence. Supposing the end state vorticity patch of a Gaussian updraft remains approximately Gaussian, we have $\nu \nabla^2 \omega_a \sim 4\nu\omega_a / l_{diff}^2$. Letting $\omega_a / \tau_{diff} \sim \nu \nabla^2 \omega_a$, our theory predicts that the vorticity will be substantially diffused over τ_{diff} time:

$$\tau_{diff} \sim \frac{l_{diff}^2}{4\nu} = \frac{\widetilde{r_u}^2}{4\nu} e^{\widetilde{\Delta h}/H}. \tag{B2}$$

We use a WTGE numerical simulation to demonstrate the damping by diffusion. A single updraft using the reference test value is put in the middle of a square domain with side length $L = 120$ km and a 256×256 mesh. The time step is 52.11 s. Let $\omega_{a,0} = f_0$. A Laplace viscosity of $\nu = 160$ m^2 s^{-1} leads to $\tau_{diff} = 2.01 \times 10^4$ s (0.23 days). Figure 17 shows that by $0.98\tau_{diff}$ after the convective peak time $t = \widetilde{T_u}/2$, diffusion has smoothed the profile significantly.

We introduce a "vorticity-equivalent top-hat" which uses a top-hat profile to approximate the shape of the vorticity patch seen by the next convection after sufficient diffusion. We let the vorticity top-hat radius be $r_u = \alpha_r \widetilde{r_u}$ where α_r is a free parameter.

Whether the patch will be significantly flattened by diffusion depends on a modified convective revisit time $\tau_{rev,m} = (-m\delta_0)^{-1}$ which is the convective interval for an air column to get involved in m updrafts during one system convergence time scale $-\delta_0^{-1}$. The interval is shorter for lucky columns that receive multiple updrafts. Its ratio to τ_{diff} is:

$$\frac{\tau_{rev,m}}{\tau_{diff}} = \frac{4\nu}{-\delta_0 \widetilde{r_u}^2} \frac{e^{-\frac{\widetilde{\Delta h}}{H}}}{m} = 4\left(-\frac{\delta_0}{f_0}\right)^{-1} \mathrm{Re}^{-1} \left(\frac{\widetilde{r_u}^2}{R^2}\right)^{-1} \frac{e^{-\frac{\widetilde{\Delta h}}{H}}}{m}. \tag{B3}$$

We get $\tau_{rev,m}/\tau_{diff} = 4.4/m$ for the reference test, where m is shown in section 6a to be typically smaller than 5. Thus, diffusion could significantly flatten the shape before the next convection occurs. The ratio is larger for lower Re and higher $-\widetilde{\Delta h}/H$, but in their sensitivity tests in section 6a, a fixed α_r works well in the vorticity PDF model. We try to explain such insensitivity as an automatic damping mechanism. Suppose multiple updrafts happen to fully or partially fall on the same vortical patch within a short time: the patch size will be several times smaller than l_{diff}, so diffusion may serve as a "peak limiter" that preferentially damps the "lucky" high vorticity patches.

APPENDIX C

A refined model of the MCS-average vorticity ω^+

We extend this problem to a finite domain to account for the situation where multiple MCS are not that far from each other, and for the artificial doubly-periodic domain effect in simulations. A fixed δ_0 and Rayleigh drag are used. We solve both ω^+ and the mean relative vorticity outside of the MCS: ω^-. We ask: how large a domain is needed to neglect the influence of compensating divergence on ω^+?

First, we introduce the MCS region net convergence ($-\delta_0^+$) that considers radiative cooling within it:

$$\delta_0^+ = \delta_0 \left(1 - \frac{S^+}{S^+ + S^-}\right), \tag{C1}$$

where $S^+ = \pi R^2$ and $S^- = L^2 - S^+$ is the area of the MCS and that outside of the MCS respectively. Performing area integration on the relative vorticity equation (6) (in flux form) within the MCS region, we get:

$$\frac{d\omega^+}{dt} = -\frac{1}{\pi R^2}\oint_{MCS} u_r \omega dl - f_0\delta_0^+ - \frac{\omega^+}{\tau_d} \approx -\frac{2}{R}u_{rb}\omega^- - f_0\delta_0^+ - \frac{\omega^+}{\tau_d}. \tag{C2}$$

Here u_{rb} is the mean radial inflow velocity at the MCS boundary obtained from Gauss' theorem. Note that the formulation of (C2) strictly only works under WTG. For SWE, the system-averaged divergence does not exactly equal to δ_0^+ due to the build up of layer thickness anomaly (warm core). We have assumed the inflow vorticity value is equal to ω^-, which is related to ω^+ by enforcing zero total relative vorticity of the doubly-periodic domain:

$$S^-\omega^- + S^+\omega^+ = 0 \quad \text{and} \quad u_{rb} = \frac{\delta_0^+ R}{2}. \tag{C3}$$

Thus, a larger domain relative to the MCS region leads to a more dilute descent, a smaller magnitude of ω^-, and a more negligible inflow vorticity flux. The horizontal eddy mixing inside the MCS only redistributes vorticity there, so it does not influence ω^+ and ω^-. Substituting (C3) into (C2), we obtain an ordinary differential equation for ω^+:

$$\frac{d\omega^+}{dt} = -\frac{\omega^+}{\tau_d^+} - f_0\delta_0^+, \quad \text{with} \quad \tau_d^+ = \left(-\delta_0^+\frac{S^+}{S^-} + \frac{1}{\tau_d}\right)^{-1}. \tag{C4}$$

Here τ_d^+ is an effective damping time scale of ω^+. With zero relative vorticity as the initial condition, the solution is:

$$\frac{\omega^+}{f_0} = -\delta_0^+\tau_d^+\left(1 - e^{-t/\tau_d^+}\right). \tag{C5}$$

When the MCS only takes a small fraction of the domain and the Rayleigh drag is not considered, τ_d^+ is much longer than the system development time scale $-\delta_0^{-1}$. In this case, the lowest order approximation is $\omega^+/f_0 \approx -\delta_0^+ t$, and the more exact solution in (C5) has a small curvature due to the local descent and the inflow of negative vorticity into the MCS. Figure 2a shows that the ω^+ of the WTGE for both the reference and the drag sensitivity test ($-\delta_0\tau_d = 2$) are in good agreement with (C5). There is no discernible difference between SWE and WTGE on the reference test, which validates the WTG approximation on the system scale. In all cases, we have $\omega^- \ll f_0$ for both SWE and WTGE. Thus, our $R/L = 1/8$ setup is large enough for the vorticity transported into the MCS to be close to 0, a property used by the vorticity PDF model in section 5.

Acknowledgments. The MATLAB code for the one layer numerical simulation and postprocessing, the namelist and initial sounding of the CM1 simulation, a derivation note, as well as a movie of the one-layer simulation can be downloaded at https://stanford.box.com/s/4g93mzxruh46ymjp2dsujkmzbbqp91gy. We are grateful to Prof. Sanjiva Lele and Prof. Nicholas Ouellette at Stanford University, Prof. Martin Singh at Monash University and Yunjiao Pu at Duke University for providing insightful comments. We thank Stanford University and Stanford Research Computing Center for providing computational resources and funding. In the end, we wish our friend Prof. Adam Showman, who is far away, could receive our gratitude for his kind help.

References

AMS-Glossary, 2012: Glossary of meteorology, american meteorological society. *URl: http://glossary. ametsoc. org/wiki/Reynolds_stresses*.

Bell, M. M., and M. T. Montgomery, 2019: Mesoscale processes during the genesis of hurricane karl (2010). *J. Atmos. Sci.*, **76 (8)**, 2235–2255.

Bister, M., and K. A. Emanuel, 1997: The genesis of hurricane guillermo: Texmex analyses and a modeling study. *Mon. Wea. Rev.*, **125 (10)**, 2662–2682.

Boubnov, B., and G. Golitsyn, 1986: Experimental study of convective structures in rotating fluids. *J. Fluid Mech.*, **167**, 503–531.

Bryan, G. H., and J. M. Fritsch, 2002: A benchmark simulation for moist nonhydrostatic numerical models. *Mon. Wea. Rev.*, **130 (12)**, 2917–2928.

Bryan, G. H., and R. Rotunno, 2009: The maximum intensity of tropical cyclones in axisymmetric numerical model simulations. *Mon. Wea. Rev.*, **137 (6)**, 1770–1789.

Charney, J. G., and A. Eliassen, 1964: On the growth of the hurricane depression. *J. Atmos. Sci.*, **21 (1)**, 68–75.

Davis, C. A., 2015: The formation of moist vortices and tropical cyclones in idealized simulations. *J. Atmos. Sci.*, **72 (9)**, 3499–3516.

Dritschel, D., and D. Waugh, 1992: Quantification of the inelastic interaction of unequal vortices in two-dimensional vortex dynamics. *Phys. Fluids*, **4 (8)**, 1737–1744.

Dritschel, D. G., 1990: The stability of elliptical vortices in an external straining flow. *J. Fluid Mech.*, **210**, 223–261.

Dunkerton, T. J., M. T. Montgomery, and Z. Wang, 2009: Tropical cyclogenesis in a tropical wave critical layer: easterly waves. *Atmos. Chem. Phys*, **9 (15)**, 5587–5646, doi:10.5194/acp-9-5587-2009, URL https://www.atmos-chem-phys.net/9/5587/2009/.

Durran, D. R., 2010: *Numerical methods for fluid dynamics: With applications to geophysics*, Vol. 32. Springer Science & Business Media.

Emanuel, K. A., 1986: An air-sea interaction theory for tropical cyclones. Part I: Steady-state maintenance. *J. Atmos. Sci.*, **43 (6)**, 585–605.

Emanuel, K. A., 1989: The finite-amplitude nature of tropical cyclogenesis. *J. Atmos. Sci.*, **46 (22)**, 3431–3456.

Emanuel, K. A., 1994: *Atmospheric convection*. Oxford University Press on Demand.

Emanuel, K. A., 1997: Some aspects of hurricane inner-core dynamics and energetics. *J. Atmos. Sci.*, **54 (8)**, 1014–1026.

Enagonio, J., and M. T. Montgomery, 2001: Tropical cyclogenesis via convectively forced vortex rossby waves in a shallow water primitive equation model. *J. Atmos. Sci.*, **58 (7)**, 685–706.

Fang, J., and F. Zhang, 2011: Evolution of multiscale vortices in the development of Hurricane Dolly (2008). *J. Atmos. Sci.*, **68 (1)**, 103–122.

Ferreira, R. N., W. H. Schubert, and J. J. Hack, 1996: Dynamical aspects of twin tropical cyclones associated with the Madden–Julian oscillation. *J. Atmos. Sci.*, **53 (7)**, 929–945.

Fritsch, J., J. Murphy, and J. Kain, 1994: Warm core vortex amplification over land. *J. Atmos. Sci.*, **51 (13)**, 1780–1807.

Gray, W. M., 1998: The formation of tropical cyclones. *Meteor. Atmos. Phys.*, **67 (1-4)**, 37–69.

Haerter, J. O., 2019: Convective Self-Aggregation As a Cold Pool-Driven Critical Phenomenon. *Geophys. Res. Lett.*, **46 (7)**, 4017–4028.

Hendricks, E. A., M. T. Montgomery, and C. A. Davis, 2004: The role of "vortical" hot towers in the formation of tropical cyclone diana (1984). *J. Atmos. Sci.*, **61 (11)**, 1209–1232.

Hendricks, E. A., W. H. Schubert, Y.-H. Chen, H.-C. Kuo, and M. S. Peng, 2014: Hurricane eyewall evolution in a forced shallow-water model. *J. Atmos. Sci.*, **71 (5)**, 1623–1643.

Holloway, C. E., A. A. Wing, S. Bony, C. Muller, H. Masunaga, T. S. L'Ecuyer, D. D. Turner, and P. Zuidema, 2017: Observing convective aggregation. *Surv Geophys*, **38 (6)**, 1199–1236.

Houze Jr, R. A., W.-C. Lee, and M. M. Bell, 2009: Convective contribution to the genesis of hurricane ophelia (2005). *Mon. Wea. Rev.*, **137 (9)**, 2778–2800.

Hsieh, T.-L., G. A. Vecchi, W. Yang, I. M. Held, and S. T. Garner, 2020: Large-scale control on the frequency of tropical cyclones and seeds: a consistent relationship across a hierarchy of global atmospheric models. *Climate Dynamics*, **55 (11)**, 3177–3196.

Julien, K., S. Legg, J. McWilliams, and J. Werne, 1999: Plumes in rotating convection. part 1. ensemble statistics and dynamical balances. *J. Fluid Mech.*, **391**, 151–187.

Khairoutdinov, M., and K. Emanuel, 2013: Rotating radiative-convective equilibrium simulated by a cloud-resolving model. *Journal of Advances in Modeling Earth Systems*, **5 (4)**, 816–825.

Kilroy, G., and R. K. Smith, 2017: The effects of initial vortex size on tropical cyclogenesis and intensification. *Quart. J. Roy. Meteor. Soc.*, **143 (708)**, 2832–2845.

Kilroy, G., R. K. Smith, and M. T. Montgomery, 2017: A unified view of tropical cyclogenesis and intensification. *Quart. J. Roy. Meteor. Soc.*, **143 (702)**, 450–462.

Kilroy, G., R. K. Smith, and U. Wissmeier, 2014: Tropical convection: The effects of ambient vertical and horizontal vorticity. *Quart. J. Roy. Meteor. Soc.*, **140 (682)**, 1756–1770.

Lahaye, N., and V. Zeitlin, 2016: Understanding instabilities of tropical cyclones and their evolution with a moist convective rotating shallow-water model. *J. Atmos. Sci.*, **73 (2)**, 505–523.

Lundgren, T., 1982: Strained spiral vortex model for turbulent fine structure. *Phys. Fluids*, **25 (12)**, 2193–2203.

McWilliams, J. C., 1990: The vortices of two-dimensional turbulence. *J. Fluid Mech.*, **219**, 361–385.

Middlebrooke, M. G., 1988: Investigation of tropical cyclone genesis and development using low-level aircraft flight data. *Atmospheric science paper; no. 429*.

Montgomery, M., M. Nicholls, T. Cram, and A. Saunders, 2006: A vortical hot tower route to tropical cyclogenesis. *J. Atmos. Sci.*, **63 (1)**, 355–386.

Montgomery, M. T., and R. K. Smith, 2014: Paradigms for tropical cyclone intensification. *Australian Meteorological and Oceanographic Journal*, **64 (1)**, 37–66.

Montgomery, M. T., and R. K. Smith, 2017: Recent developments in the fluid dynamics of tropical cyclones. *Annual Review of Fluid Mechanics*, **49**, 541–574.

Montgomery, M. T., H. D. Snell, and Z. Yang, 2001: Axisymmetric spindown dynamics of hurricane-like vortices. *J. Atmos. Sci.*, **58 (5)**, 421–435.

Morrison, H., J. Curry, and V. Khvorostyanov, 2005: A new double-moment microphysics parameterization for application in cloud and climate models. part i: Description. *J. Atmos. Sci.*, **62 (6)**, 1665–1677.

Muller, C. J., and D. M. Romps, 2018: Acceleration of tropical cyclogenesis by self-aggregation feedbacks. *Proc. Natl. Acad. Sci. USA*, **115 (12)**, 2930–2935.

Neelin, J. D., and I. M. Held, 1987: Modeling tropical convergence based on the moist static energy budget. *Mon. Wea. Rev.*, **115 (1)**, 3–12.

Ooyama, K., 1969: Numerical simulation of the life cycle of tropical cyclones. *J. Atmos. Sci.*, **26 (1)**, 3–40.

O'Neill, M. E., K. A. Emanuel, and G. R. Flierl, 2015: Polar vortex formation in giant-planet atmospheres due to moist convection. *Nature Geoscience*, **8 (7)**, 523–526.

O'Neill, M. E., K. A. Emanuel, and G. R. Flierl, 2016: Weak jets and strong cyclones: Shallow-water modeling of giant planet polar caps. *J. Atmos. Sci.*, **73 (4)**, 1841–1855.

Pasquero, C., and G. Falkovich, 2002: Stationary spectrum of vorticity cascade in two-dimensional turbulence. *Phys. Rev. E*, **65 (5)**, 056 305.

Peters, J. M., C. J. Nowotarski, and G. L. Mullendore, 2020: Are supercells resistant to entrainment because of their rotation? *J. Atmos. Sci.*, **77 (4)**, 1475–1495.

Pishro-Nik, H., 2014: *Introduction to Probability, Statistics, and Random Processes*. Kappa Research, LLC, URL https://books.google.com/books?id=3yq_oQEACAAJ.

Pope, S. B., 2001: *Turbulent flows*. IOP Publishing.

Raymond, D. J., S. L. Sessions, and Ž. Fuchs, 2007: A theory for the spinup of tropical depressions. *Quart. J. Roy. Meteor. Soc.*, **133 (628)**, 1743–1754.

Ritchie, E. A., and G. J. Holland, 1997: Scale interactions during the formation of typhoon irving. *Mon. Wea. Rev.*, **125 (7)**, 1377–1396.

Ritchie, E. A., and G. J. Holland, 1999: Large-scale patterns associated with tropical cyclogenesis in the western Pacific. *Mon. Wea. Rev.*, **127 (9)**, 2027–2043.

Rotunno, R., and K. A. Emanuel, 1987: An air–sea interaction theory for tropical cyclones. Part II: Evolutionary study using a nonhydrostatic axisymmetric numerical model. *J. Atmos. Sci.*, **44 (3)**, 542–561.

Schecter, D. A., 2017: A computational study on the nature of meso-β scale vortex coalescence in a tropical atmosphere. *J. Adv. Model. Earth Syst.*, **9 (2)**, 1366–1398.

Schecter, D. A., and T. J. Dunkerton, 2009: Hurricane formation in diabatic Ekman turbulence. *Quart. J. Roy. Meteor. Soc.*, **135 (641)**, 823–838.

Schubert, W. H., M. T. Montgomery, R. K. Taft, T. A. Guinn, S. R. Fulton, J. P. Kossin, and J. P. Edwards, 1999: Polygonal eyewalls, asymmetric eye contraction, and potential vorticity mixing in hurricanes. *J. Atmos. Sci.*, **56 (9)**, 1197–1223.

Showman, A. P., 2007: Numerical simulations of forced shallow-water turbulence: Effects of moist convection on the large-scale circulation of Jupiter and Saturn. *J. Atmos. Sci.*, **64 (9)**, 3132–3157.

Smith, R. K., 2000: The role of cumulus convection in hurricanes and its representation in hurricane models. *Rev. Geophys.*, **38 (4)**, 465–489.

Smith, W. P., and M. E. Nicholls, 2019: On the creation and evolution of small-scale low-level vorticity anomalies during tropical cyclogenesis. *J. Atmos. Sci.*, **76 (8)**, 2335–2355.

Sobel, A. H., J. Nilsson, and L. M. Polvani, 2001: The weak temperature gradient approximation and balanced tropical moisture waves. *J. Atmos. Sci.*, **58 (23)**, 3650–3665.

Sukhatme, J., and W. R. Young, 2011: The advection–condensation model and water-vapour probability density functions. *Quart. J. Roy. Meteor. Soc.*, **137 (659)**, 1561–1572.

Tennekes, H., and J. L. Lumley, 2018: *A first course in turbulence*. MIT press.

Terwey, W. D., and M. T. Montgomery, 2008: Secondary eyewall formation in two idealized, full-physics modeled hurricanes. *J. Geophys. Res.*, **113 (D12)**.

Thom, H. C. S., 1957: The frequency of hail occurrence. *Archiv für Meteorologie, Geophysik und Bioklimatologie, Serie B*, **8 (2)**, 185–194.

Thomson, S. I., and M. E. McIntyre, 2016: Jupiter's unearthly jets: A new turbulent model exhibiting statistical steadiness without large-scale dissipation. *J. Atmos. Sci.*, **73 (3)**, 1119–1141.

Torri, G., and Z. Kuang, 2019: On cold pool collisions in tropical boundary layers. *Geophys. Res. Lett.*, **46 (1)**, 399–407.

Vallis, G., G. Shutts, and M. Gray, 1997: Balanced mesoscale motion and stratified turbulence forced by convection. *Quart. J. Roy. Meteor. Soc.*, **123 (542)**, 1621–1652.

Vallis, G. K., 2017: *Atmospheric and oceanic fluid dynamics*. Cambridge University Press.

Van Sang, N., R. K. Smith, and M. T. Montgomery, 2008: Tropical-cyclone intensification and predictability in three dimensions. *Quart. J. Roy. Meteor. Soc.*, **134 (632)**, 563–582.

Wang, Y., 2002a: Vortex rossby waves in a numerically simulated tropical cyclone. part i: Overall structure, potential vorticity, and kinetic energy budgets. *J. Atmos. Sci.*, **59 (7)**, 1213–1238.

Wang, Y., 2002b: Vortex rossby waves in a numerically simulated tropical cyclone. part ii: The role in tropical cyclone structure and intensity changes. *J. Atmos. Sci.*, **59 (7)**, 1239–1262.

Wang, Y., and G. J. Holland, 1995: On the interaction of tropical-cyclone-scale vortices. IV: Baroclinic vortices. *Quart. J. Roy. Meteor. Soc.*, **121 (521)**, 95–126.

Wang, Y., L. Zhang, J. Peng, and S. Liu, 2018: Mesoscale horizontal kinetic energy spectra of a tropical cyclone. *J. Atmos. Sci.*, **75 (10)**, 3579–3596.

Wing, A. A., S. J. Camargo, and A. H. Sobel, 2016: Role of radiative–convective feedbacks in spontaneous tropical cyclogenesis in idealized numerical simulations. *J. Atmos. Sci.*, **73 (7)**, 2633–2642.

Wissmeier, U., and R. K. Smith, 2011: Tropical cyclone convection: The effects of ambient vertical vorticity. *Quart. J. Roy. Meteor. Soc.*, **137 (657)**, 845–857.

Würsch, M., and G. C. Craig, 2014: A simple dynamical model of cumulus convection for data assimilation research. *Meteorol. Z.*, **(5)**, 483–490.

LIST OF FIGURES

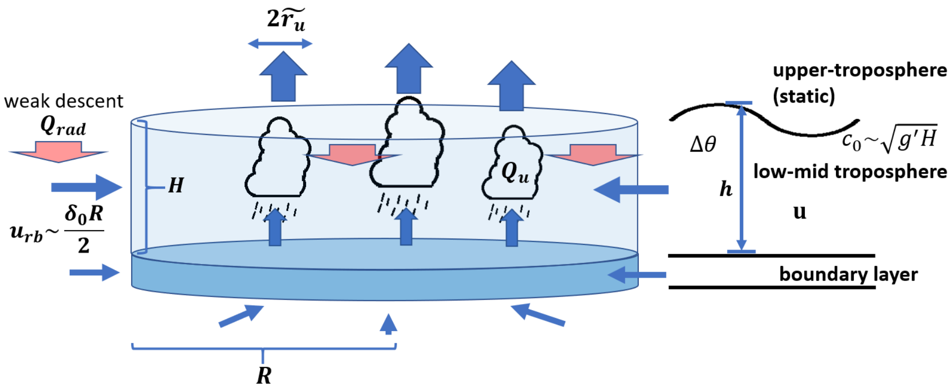

FIG. 1. A schematic diagram of the mesoscale convective system (MCS) and the shallow water setup which depicts the low-mid troposphere. Deep convection only occurs in the MCS. The air entrained by convection to the upper-troposphere is compensated by the horizontal inflow which is driven by radiative cooling in the whole domain.

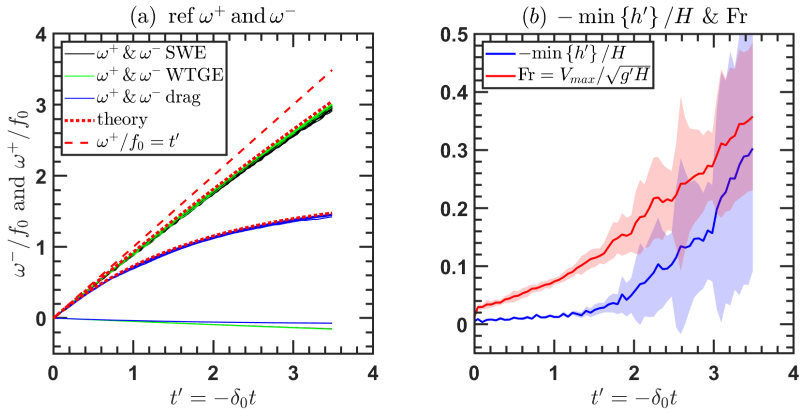

FIG. 2. (a) The time evolution of the mean vorticity in the MCS (ω^+) and out of the MCS (ω^-) for an ensemble of 20 runs of the SWE reference test (20 solid black lines), the WTGE reference test (20 solid green lines), the $-\delta_0\tau_d = 2$ drag sensitivity test (20 solid blue lines), the finite-domain theory of ω^+ in (C5) for both the reference and drag test (the two dotted red lines), and the approximate solution $\omega^+/f_0 = -\delta_0 t$ (the dashed red line). Note that all of the ω^+/f_0 data is positive, and that of ω^-/f_0 is negative. The temporal coordinate t' is the time nondimensionalized with the MCS mean divergence: $t' = -\delta_0 t$. (b) The blue line shows the time evolution of the domain minimum thickness disturbance normalized by basic state thickness: $-\min\{h'/H\}$ for an ensemble of 20 runs of the SWE reference test (Ref-SWE). The red line shows the ensemble-averaged $\mathrm{Fr} = V_{max}/\sqrt{g'H}$, where V_{max} is the maximum total wind. The shadow denotes the ± 1 standard deviation range. For both (a) and (b), only the data of $0 \leq t' \leq 3.56$ are plotted, because one SWE run blows up after that, due to the computational instability induced by the sharp vorticity gradient.

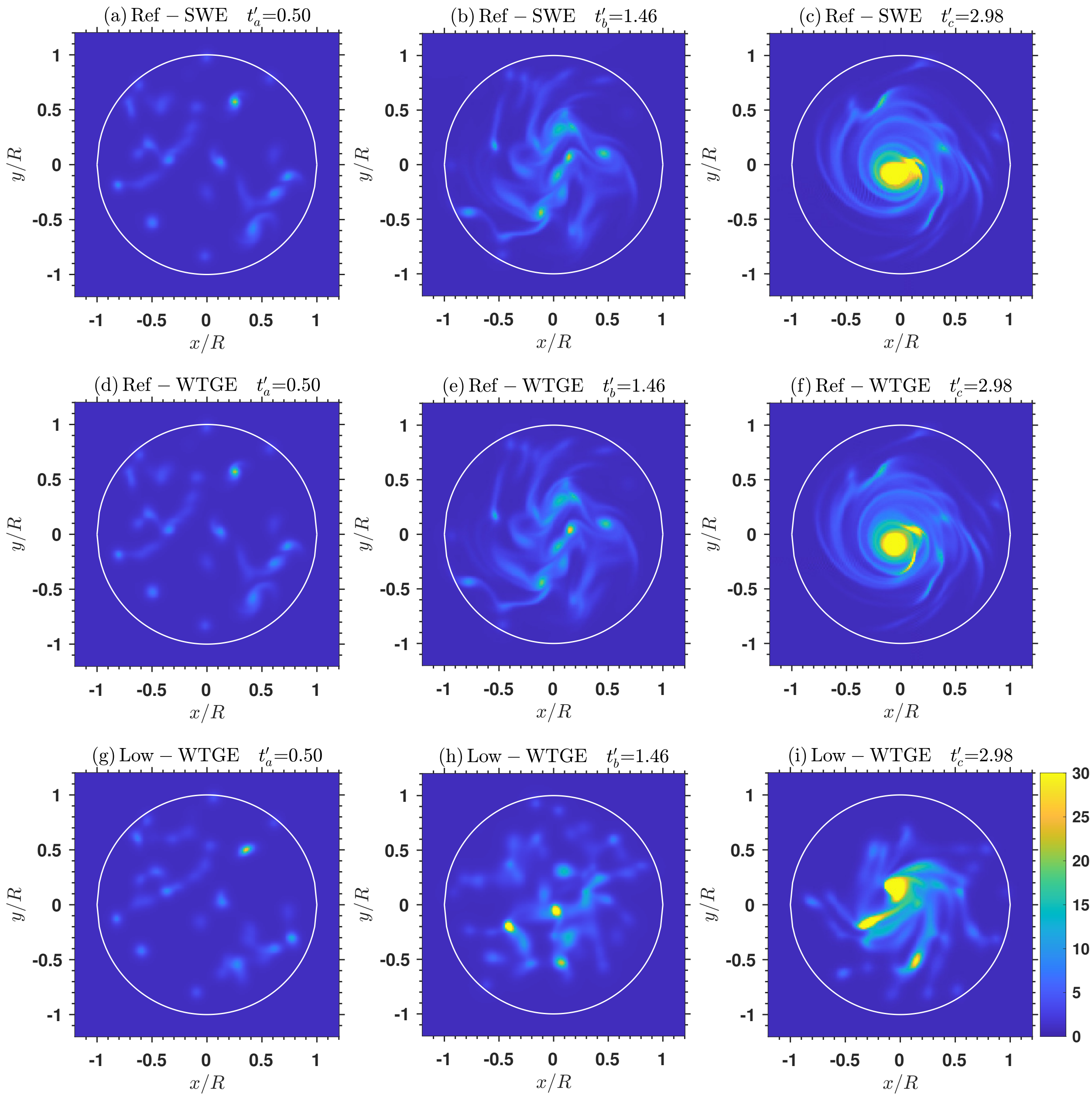

FIG. 3. An example of ω_a/f_0 for Ref-SWE (upper row), Ref-WTGE (middle row) and Low-WTGE (lower row, $\delta_0/f_0 \times 10$). For each test, only the ensemble index 1 among of the 20-member ensemble is shown. The convective seeding history of the three runs are identical. The $t_a' = -\delta_0 t = 0.50$ snapshot is at the left column, the $t_b' = 1.46$ is at the middle column, and the $t_c' = 2.98$ is at the right column. The white circle is the MCS boundary. The spatial coordinate has been normalized by R.

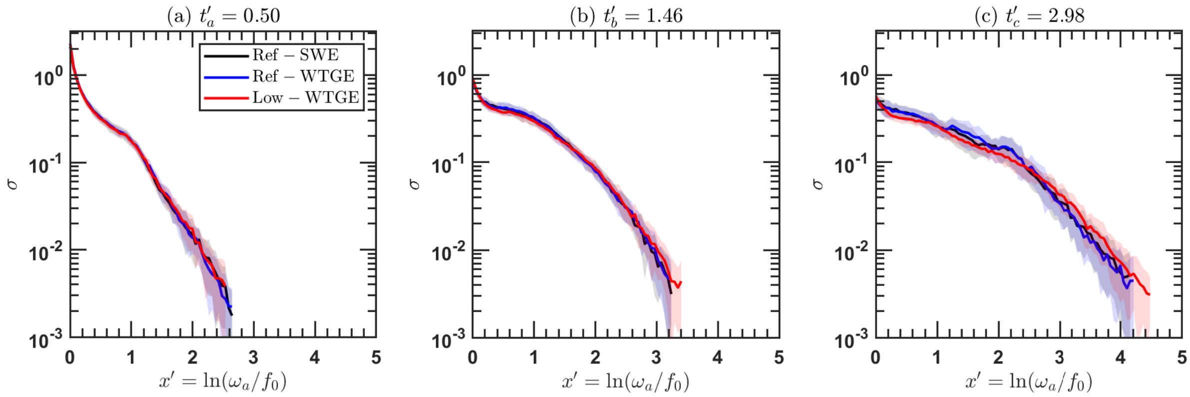

1244 FIG. 4. The comparison of vorticity PDF of Ref-SWE, Ref-WTGE and Low-WTGE ($\delta_0/f_0 \times 10$) for the
1245 reference test at (a) $t'_a = 0.50$, (b) $t'_b = 1.46$ and (c) $t'_c = 2.98$. The colored shadow denotes the ± 1 standard
1246 deviation of the 20-member ensemble of each test. The black, blue and red lines are the ensemble average
1247 of Ref-SWE, Ref-WTGE and Low-WTGE. The PDF from simulation is cutoff at the bin where the standard
1248 deviation is larger than the ensemble average. Only the $x' = \ln(\omega_a/f_0) > 0$ bins are shown.

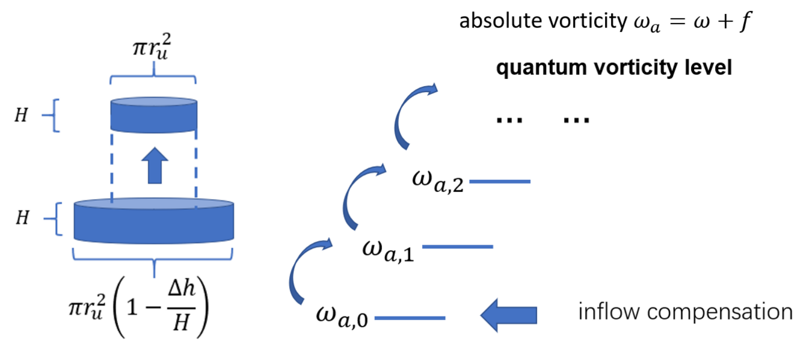

FIG. 5. A schematic diagram for the migration of air columns on the vorticity level system $\omega_{a,m} = \omega_{a,0}(1 - \Delta h/H)^m$ due to vorticity stretching, where $\omega_{a,0} = f_0$. A column can only jump one level upward in a single updraft event.

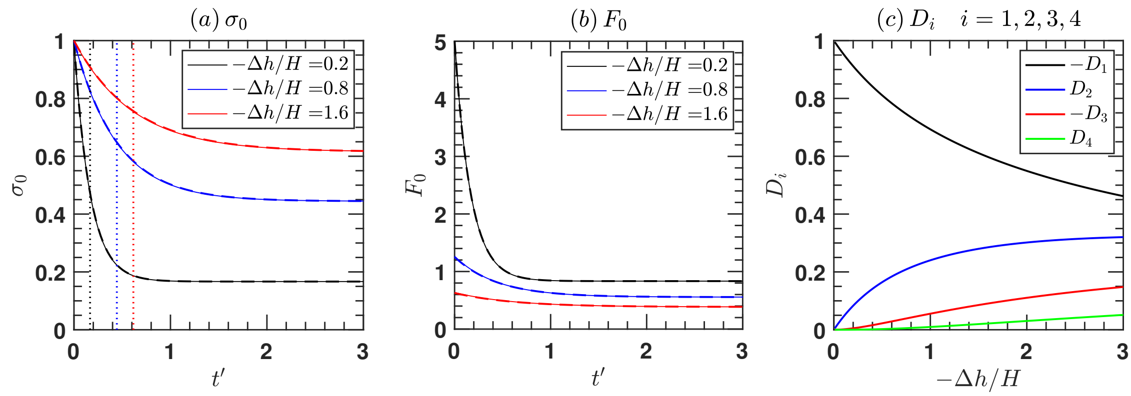

FIG. 6. (a) the evolution of the $\omega_a = f_0$ basic level PDF value σ_0 with nondimensional time for $-\Delta h/H = 0.2$, 0.8 and 1.6, denoted by the black, blue and red lines respectively. The solid lines are for $r_u = 8\sqrt{2}$ km (reference value), and the dashed lines are for $r_u = 4\sqrt{2}$ km. They collapse well. The dotted lines are the nondimensional adjustment time scale $-\delta_0\tau_{\sigma_0} = (-\Delta h/H)/(1-\Delta h/H)$. (b) The same as (a), but for the probability current F_0 which is the F at $x' = \Delta x'/2$. (c) The dependence of the PDF equation coefficients D_1, D_2, D_3 and D_4 on $-\Delta h/H$, denoted as the black, blue, red and green line respectively. As D_1 and D_3 are negative, we plot $-D_1$ and $-D_3$ to ease visualization.

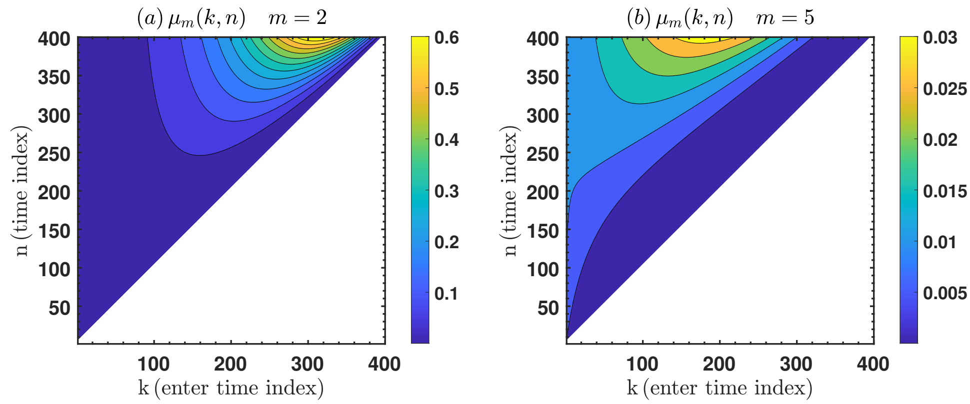

FIG. 7. The fractional contribution μ_k to σ_m^n for different ages of air columns predicted by the theory, using the reference test parameter. The horizontal axis is the time index k on which the column enters MCS, and the vertical axis is the time index n. The blank region denotes $\mu_k = 0$. The subplot (a) shows the $m = 2$ vorticity level and (b) shows the $m = 5$ level. Note that both n and k are positive integers. Only $k \geq 1$ columns which are not originally inside the MCS are plotted.

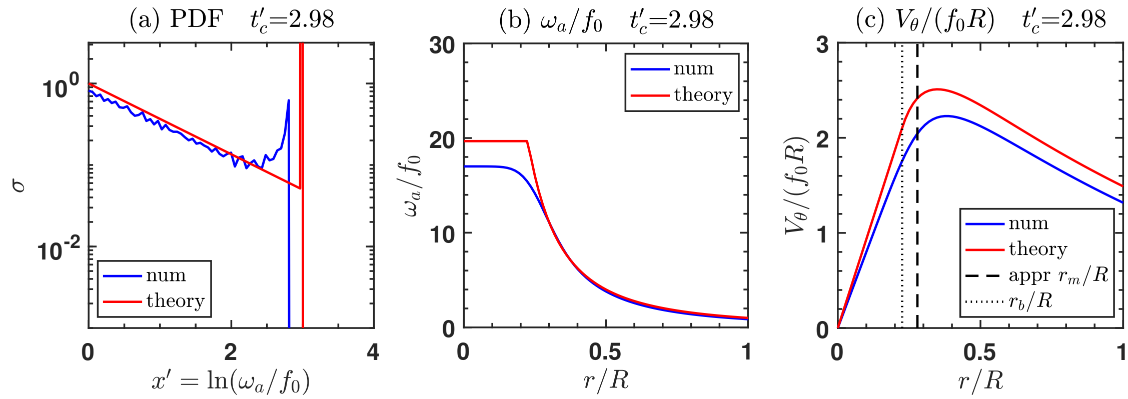

FIG. 8. The $-\Delta h/H \to 0$ problem. (a) The blue line is the vorticity PDF diagnosed from the grid point data of the numerical simulation with the reference value Re, and the red line is the direct analytical solution of the PDF shown in (33). (b) A radial cross-section of the axisymmetric vorticity field of the of the uniform forcing test ($-\Delta h/H \to 0$) at $t'_c = 2.98$. The blue line is the numerical solution, and the red line is the analytical solution. The difference is mainly due to viscosity and the finite-domain effect. (c) The same as (b), but for the local Rossby number: $V_\theta/(f_0R)$. The approximate expression of the radius of maximum wind: $r_m \approx r_b[1+(1-e^{-t'})/4]$, and the vortex core radius r_b, both normalized by R, are additionally plotted as the dashed black line and the dotted black line respectively.

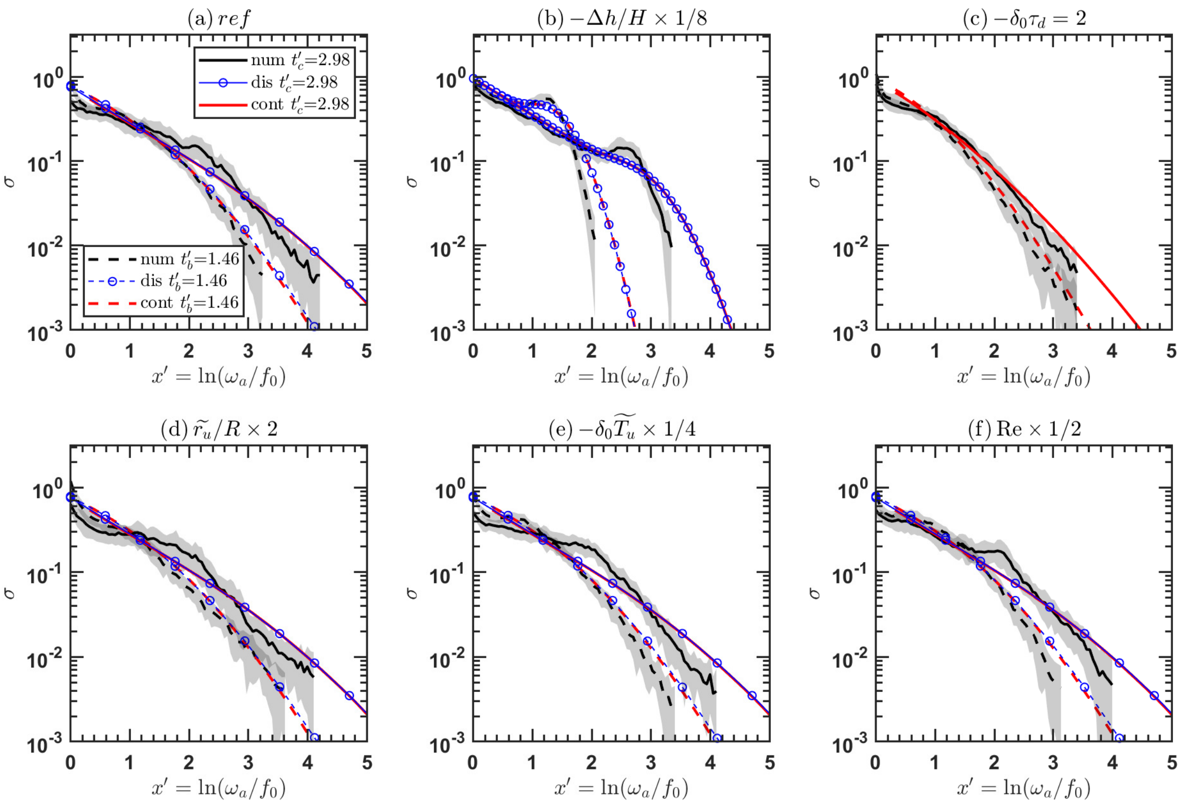

FIG. 9. The vorticity PDF of the six WTGE tests at $t'_b = 1.46$ and $t'_c = 2.98$, of (a) the reference test, (b) the $-\Delta h/H \times 1/8$ and $-\delta_0 \widetilde{T}_u \times 1/8$ test, (c) the $-\delta_0 \tau_d = 2$ test, (d) the $\widetilde{r}_u/R \times 2$ test, (e) the $-\delta_0 \widetilde{T}_u \times 1/4$ test and (f) the Re $\times 1/2$ test. The grey shadow is the ± 1 standard deviation of the ensemble runs. The black line is the ensemble average in each test, the blue circle line is the analytical solution of the discrete PDF shown in (24) which uses the time index n closest to the inquired time, and the red line is the numerical solution of the continuous part (σ_c) of the hybrid PDF problem. The discrete PDF model of the τ_d test is unavailable. For all cases, the dashed and solid lines denote $t'_b = 1.46$, and $t'_c = 2.98$ case respectively. The PDF from simulation (the black line and the shadow) is cutoff at the bin where the standard deviation is larger than the average. Only $x' = \ln(\omega_a/f_0) > 0$ bins are shown.

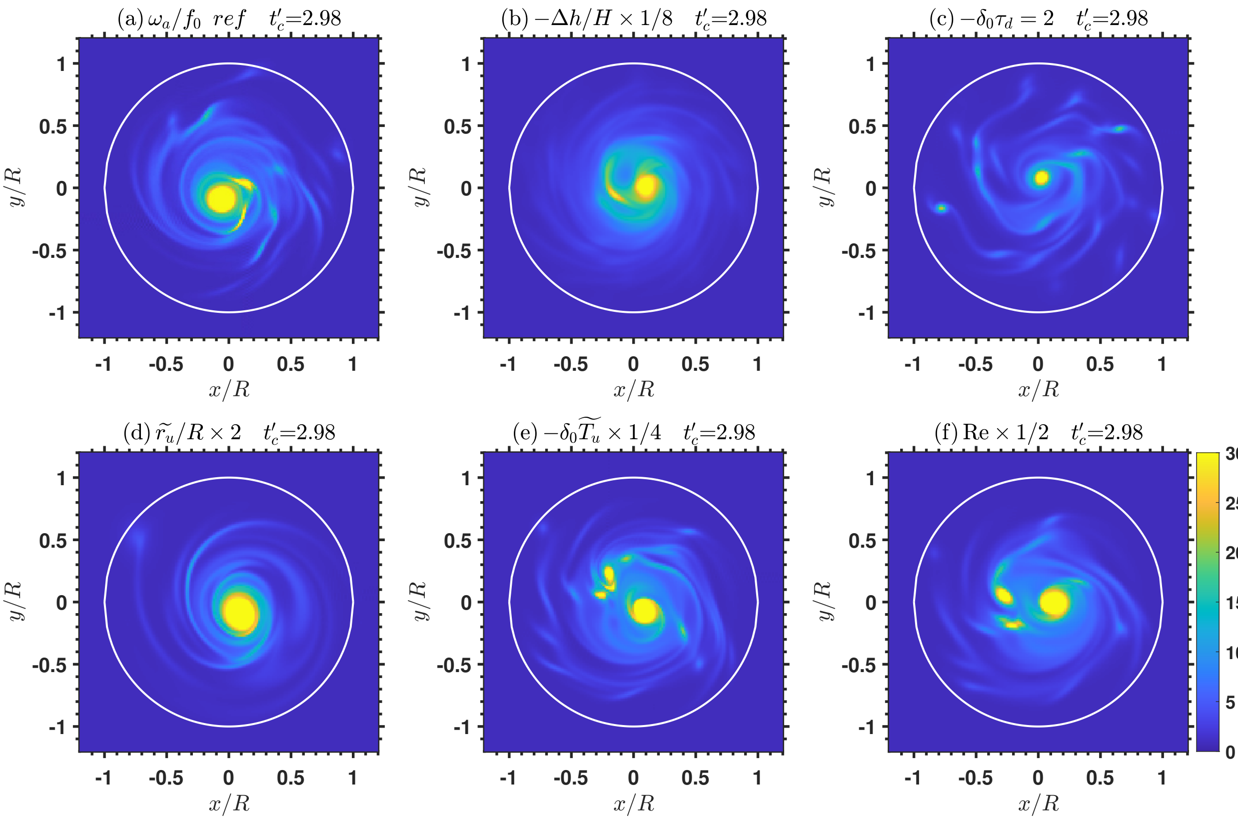

FIG. 10. An example of the ω_a/f_0 snapshot of the same six tests as Fig. 9 at $t'_c = 2.98$. The white circle is the MCS boundary. Of the 20 runs in each ensemble, only the run with ensemble index 1 is shown.

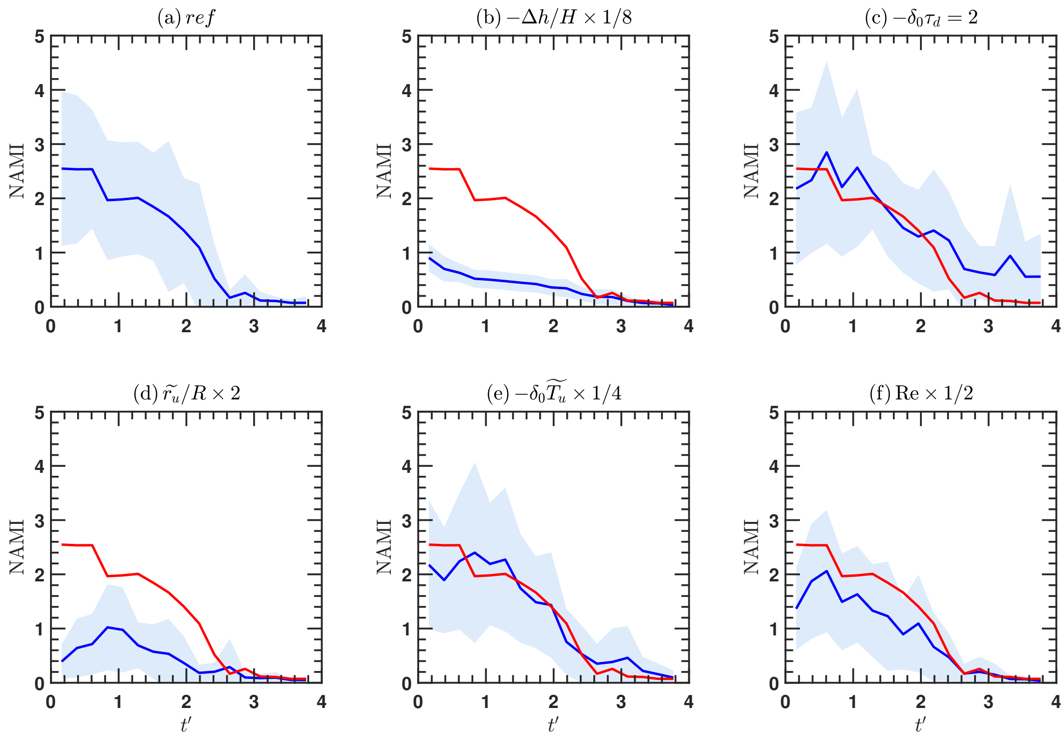

FIG. 11. The time evolution of NAMI (non-axisymmetric and monotonic index) with time for the six tests introduced in Fig. 9. The solid blue line is the ensemble average value in each test. The blue shadow denotes the ± 1 standard deviation range. The red line in (b)-(f) denotes the NAMI of the reference test, which is identical to the blue line in (a).

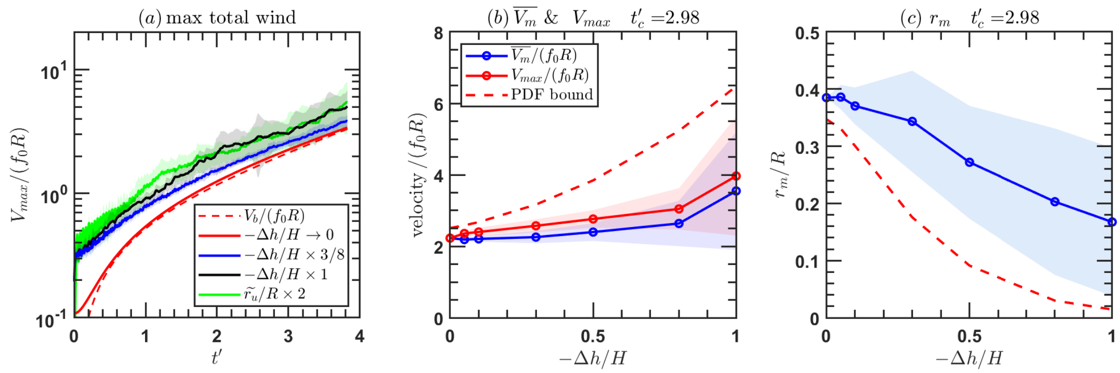

FIG. 12. (a) The solid red, blue, black and green lines denote the ensemble average of the domain maximum wind, for the $-\Delta h/H \to 0$ test (numerical solution with eddy diffusivity), the $-\Delta h/H \times 3/8$ test, the reference test and the $\widetilde{r_u}/R \times 2$ test respectively. The red dashed line denotes V_b which is the velocity at the solid rotation vortex core boundary. (b) The ensemble average of the maximum azimuthal mean azimuthal wind $\overline{V_m}$ (the blue circle line) and the maximum total wind V_{max} (the red circle line) at $t'_c = 2.98$ for simulations with different $-\Delta h/H$. The dashed red line denotes the theoretical upper bound V_{Um}. (c) The ensemble average (the blue circle line) of r_m which is the radius of $\overline{V_m}$, for different $-\Delta h/H$. The dashed red line denotes r_{Um}, which is the radius on the theoretically reconstructed profile $V_U(r)$ where V_{Um} resides. All changes on $-\Delta h/H$ are accompanied by the corresponding changes on $-\delta_0\widetilde{T_u}$ to keep the nondimensional mass sink rate $\widetilde{Q_m}/(-\delta_0 H)$ fixed. All of the shadow denotes the ± 1 standard deviation range of the 20-member ensemble.

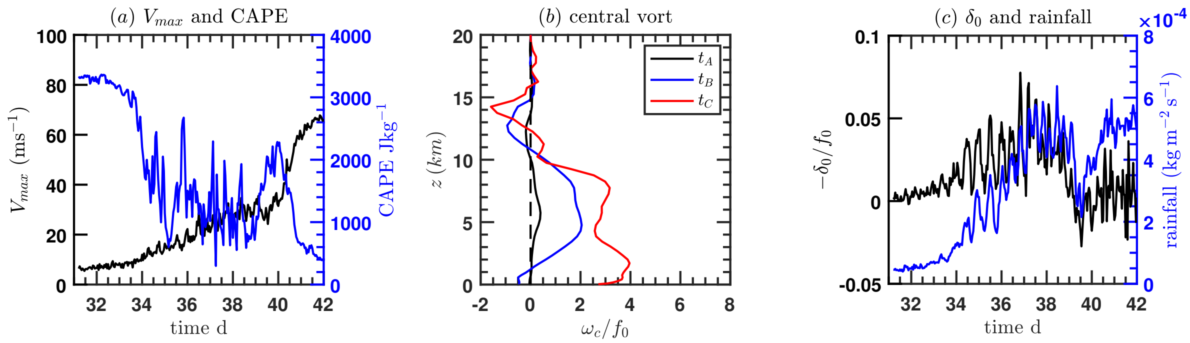

FIG. 13. (a) The black curve is the maximum absolute wind at 25 m height within the $R = 250$ km MCS. The MCS center is defined as the maximum point of the filtered low-mid level vertical vorticity, which is defined as the 1.18-6.25 km vertically averaged vertical vorticity processed with a 30 km-scale horizontal Gaussian filter. The blue curve is the time series of the 30 km-filtered convective available potential energy (CAPE) at the MCS center. (b) The vertical profile of the 30 km-filtered vertical vorticity at the MCS center ω_c normalized by f_0, with the black, blue and red curve denoting $t_A = 31.21$ days, $t_B = 34.12$ days and $t_C = 37.04$ days respectively. (c) The black curve is the time series of the MCS-averaged low-mid level (1.18-6.25 km vertically averaged) nondimensional divergence $\delta_0(t)/f_0$, and the blue curve is the rainfall rate (unit: kg m^{-2} s^{-1}).

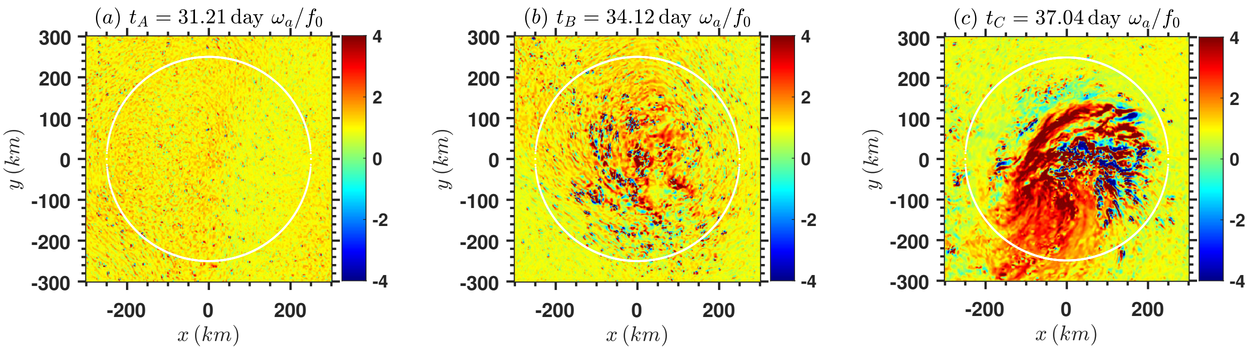

FIG. 14. The low-mid level (1.18-6.25 km vertically averaged) vertical absolute vorticity normalized by f_0 at (a) $t_A = 31.21$ days, (b) $t_B = 34.12$ days and (c) $t_C = 37.04$ days.

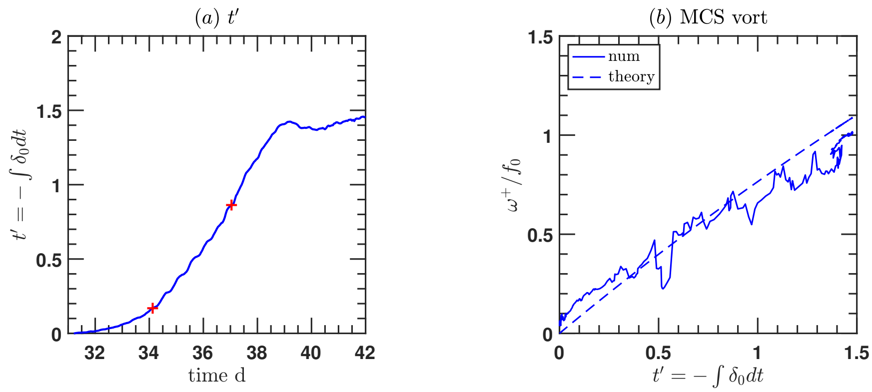

FIG. 15. (a) The blue curve is the rescaled nondimensional temporal coordinate $t' = -\int_{t_A}^{t} \delta_0(t'')dt''$ versus time t. The red "+" denotes t'_B and t'_C. (b) The evolution of MCS-averaged low-mid level vertical vorticity ω^+ in t' coordinate. The solid blue line is from the simulation, and the dashed blue line is the prediction by (40).

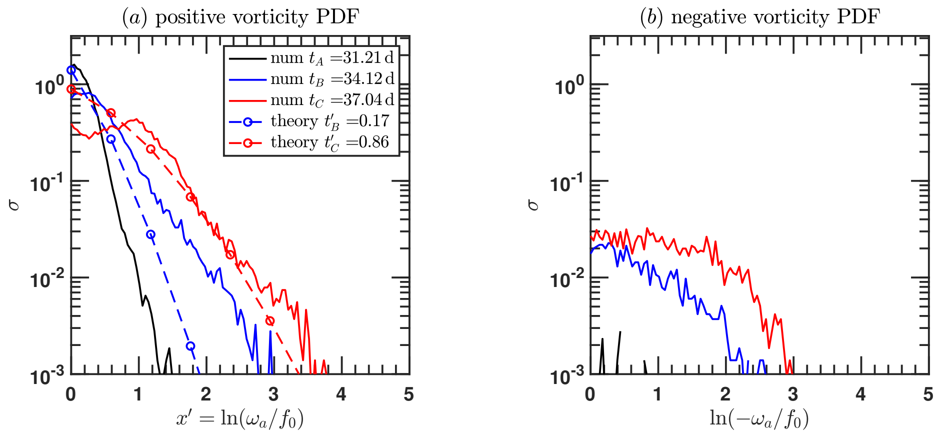

FIG. 16. The PDF of the low-mid level (1.18-6.25 km vertically averaged) vertical absolute vorticity normalized by f_0. (a) The positive vorticity side ($\omega_a > f_0$), with the solid black, blue and red lines denoting $t_A = 31.21$ days, $t_B = 34.12$ days and $t_C = 37.04$ days respectively. The rescaled nondimensional time is $t'_B = -\int_{t_A}^{t_B} \delta_0(t'')dt'' = 0.17$ and $t'_C = -\int_{t_A}^{t_C} \delta_0(t'')dt'' = 0.86$. The circled blue and red lines is the analytical solution of the discrete Markov chain shown in (24). (b) is the same as (a), but for the negative vorticity side ($\omega_a < -f_0$). The Markov chain does not predict negative vorticity bins. The weak vorticity range ($-f_0 < \omega_a < f_0$) is not shown in this figure.

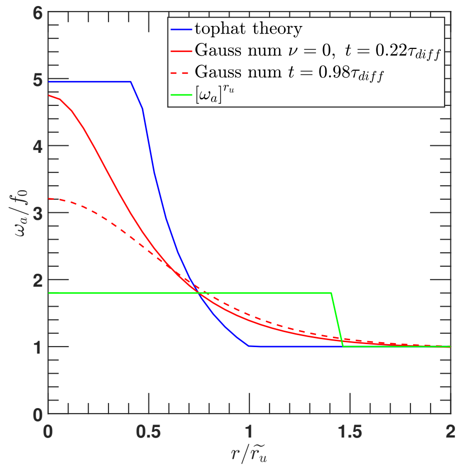

FIG. 17. The radial profile (the positive x side of the $y = 0$ cross section) of ω_a/f_0 for the single updraft test. The solid blue line is the analytical solution (B1) for the top-hat convergence profile, after the convection ends. The solid red line is an inviscid ($\nu = 0$) numerical solution of the Gaussian profile right after the convection ends. The dashed red line is a viscous ($\nu = 160$ m^2 s^{-1}) simulation at $0.98\tau_{diff}$ after the updraft peaks. The solid green line denotes the "vorticity-equivalent top-hat" profile of the vorticity patch which is used for the PDF model.

Supplement to: The role of random vorticity stretching in tropical depression genesis

Hao Fu* and Morgan O'Neill

Department of Earth System Science, Stanford University, California

**Corresponding author address:* Hao Fu, 473 Via Ortega, Stanford, CA 94305.

E-mail: haofu@stanford.edu

ABSTRACT

The derivation of the continuous PDF equation

To obtain the contribution of vorticity migration to the probability current F in the continuous PDF equation, one informal but straightforward way is to derive the modified equation of the Markov chain model using Taylor expansion, without considering Rayleigh drag. The recurrence relationship of the Markov chain in (18) can be written as:

$$\frac{\sigma_m^n - \sigma_m^{n-1}}{-\delta_0 \Delta t} = \left[\frac{r_u^2}{R^2}\frac{1}{\delta_0 \Delta t}\left(\ln\omega_{a,m} - \ln\omega_{a,m-1}\right)\right]\frac{\sigma_m^{n-1} - \sigma_{m-1}^{n-1}}{\ln\omega_{a,m} - \ln\omega_{a,m-1}} - \sigma_m^{n-1}\frac{r_u^2}{R^2}\frac{\Delta h}{H}\frac{1}{\delta_0 \Delta t}. \tag{S1}$$

Now we let $x' = \ln(\omega_a/f_0)$, $\Delta x' = x'_m - x'_{m-1} = \ln(1 - \Delta h/H)$, $t' = -\delta_0 t$ and $\Delta t' = -\delta_0 \Delta t = (-\Delta h/H)(r_u^2/R^2)$ after using (12). Using (26), (S1) can be transformed to an equation of σ_c, which can be regarded as a forward-in-time and forward-in-space discretization of an advection equation with damping:

$$\frac{\partial \sigma_c}{\partial t'} = D_1 \frac{\partial \sigma_c}{\partial x'} - \sigma_c. \tag{S2}$$

Here D_1 equals to the middle bracket of (S1), and its expression is shown in (31).

Now we derive the modified equation of (S1) via Taylor expansion (e.g. Durran 2010). The LHS of (S1) is:

$$\frac{\sigma_m^n/\Delta x' - \sigma_m^{n-1}/\Delta x'}{\Delta t'} = \frac{\partial \sigma_c}{\partial t'} + \frac{1}{2}\frac{\partial^2 \sigma_c}{\partial t'^2}\Delta t' + O(\Delta t')^2. \tag{S3}$$

Here $\partial^2 \sigma_c/\partial t'^2$ is represented by the partial derivative to x' using (S2):

$$\frac{\partial^2 \sigma_c}{\partial t'^2} = D_1 \frac{\partial^2 \sigma_c}{\partial x' \partial t'} - \frac{\partial \sigma_c}{\partial t'} = D_1^2 \frac{\partial^2 \sigma_c}{\partial x'^2} - 2D_1 \frac{\partial \sigma_c}{\partial x'} + \sigma_c, \tag{S4}$$

where D_1 equals to the middle bracket of (S1). The Taylor expansion of the first term on the RHS of (S1) is:

$$\frac{r_u^2}{R^2}\frac{\Delta x'}{\delta_0 \Delta t}\frac{\sigma_m^n/\Delta x' - \sigma_m^{n-1}/\Delta x'}{\Delta x'} \approx \sum_{i=1}^{4} D_i \frac{\partial^i \sigma_c}{\partial x'^i} + O\left(\Delta x'\right)^4. \tag{S5}$$

Here the expression of D_i is shown in (31). The σ_m^{n-1} is expanded as:

$$\frac{\sigma_m^{n-1}}{\Delta x'} \approx \frac{\sigma_m^n}{\Delta x'} - \Delta t' \frac{\partial \sigma_c}{\partial t'} + O(\Delta t')^2 = \sigma_c - \Delta t' \left(D_1 \frac{\partial \sigma_c}{\partial x'} - \sigma_c \right) + O(\Delta t')^2. \tag{S6}$$

Substituting (S3), (S4), (S5) and (S6) into (S1), we get:

$$\frac{\partial \sigma_c}{\partial t'} = -\widetilde{D_0}\sigma_c + \sum_{i=1}^{4} \widetilde{D}_i \frac{\partial^i \sigma_c}{\partial x'^i} + O\big(\Delta x'\big)^4 + O\big(\Delta t'\big)^2, \tag{S7}$$

with

$$\begin{cases} \widetilde{D_0} = 1 + \frac{3}{2}\Delta t', \\ \widetilde{D_1} = D_1(1 + 2\Delta t'), \\ \widetilde{D_2} = D_2 \left(1 - \frac{D_1^2}{D_2}\frac{\Delta t'}{2}\right) = D_2 \left(1 + \frac{r_u^2}{R^2}\right), \\ \widetilde{D_3} = D_3,\ \widetilde{D_4} = D_4. \end{cases} \tag{S8}$$

Here we have used (12) to derive $\widetilde{D_2}$. For all our tests, there is $\Delta t' = -\delta_0 \Delta t \sim 10^{-2}$, $\Delta x' \sim 1$, $r_u^2/R^2 \ll 1$. These lead to $\widetilde{D_0} \approx 1$, $\widetilde{D}_i \approx D_i$, $i = 1,2,3,4$, so there is no need to examine higher temporal expansion terms in (S3). Thus, the new updraft seeding frequency is high enough to make this system look continuous in time. However, this analysis only deals with the ensemble average of PDF. The randomness induces stronger fluctuation at high vorticity levels (bins) for larger $\Delta t'$, as is discussed in section 6a.

a. The formal derivation of the continuous PDF equation

We derive the PDF equation with the stricter random variable approach (Pope 2001). The viscous effect is neglected because we have not figured out the proper model. We introduce $f'(x';\mathbf{x},t') = \Theta(X'(\mathbf{x},t') - x')$ as the "fine-grained PDF" of $x' = \ln(\omega_a/f_0)$ in the MCS region, with $X'(\mathbf{x},t')$ as a random variable and Θ denoting Dirac-Delta function. Note that $\mathbf{x}$ is the position vector.

As vorticity is not a passive tracer, we define the dimensional velocity $\mathbf{U}(\mathbf{x},t')$ as a space-dependent random variable. Just like (7), $\mathbf{U}$ can be decomposed into a div-free component $\mathbf{U}_\omega$ which is controlled by vorticity and therefore f' (not to be confused with Coriolis parameter f_0), as well as a curl-free component $\mathbf{U}_\delta$ which is determined by the random seeding and therefore independent from f':

$$\mathbf{U} = \mathbf{U}_\omega + \mathbf{U}_\delta \quad \text{with} \quad \mathbf{U}_\omega = \mathbf{k} \times \nabla\Psi, \quad \mathbf{U}_\delta = \nabla\Phi, \tag{S9}$$

where Ψ and Φ are stream function and velocity potential as random variables. The definition of f' yields its governing equation (Pope 2001):

$$\frac{\partial f'}{\partial t'} - \frac{1}{\delta_0}\mathbf{U}\cdot\nabla f' = -\frac{\partial}{\partial x'}\left(f'\frac{DX'}{Dt'}\right), \tag{S10}$$

where $D/Dt' = \partial/\partial t' - \delta_0^{-1}\mathbf{U}\cdot\nabla$ is the normal 2D substantial derivative operator divided by $-\delta_0$. The DX'/Dt' is the nondimensional and inviscid form of the vertical vorticity equation shown in (6):

$$\frac{DX'}{Dt'} = \frac{\delta}{\delta_0} + \frac{1-e^{-X'}}{\delta_0\tau_d}. \tag{S11}$$

This is a stochastic differential equation driven by the random δ. Next, we implement an average operator, whose effect on $f'(x';\mathbf{x},t')$, an arbitrary random variable such as $G(\mathbf{x},t')$, and their product $f'G$ are:

$$\left\langle f'(x';\mathbf{x},t')\right\rangle = \int_{-\infty}^{+\infty}\Theta(x''-x')f(x'';\mathbf{x},t')dx'' = f(x';\mathbf{x},t'), \tag{S12}$$

$$\left\langle G(\mathbf{x},t')\right\rangle = \int_{-\infty}^{+\infty}G(\mathbf{x},t')f(x'';\mathbf{x},t')dx'', \tag{S13}$$

$$\begin{aligned}\left\langle f'(x';\mathbf{x},t')G(\mathbf{x},t')\right\rangle &= \int_{-\infty}^{+\infty}\Theta(x''-x')G(\mathbf{x},t')f(x'';\mathbf{x},t')dx'' \\ &= f(x';\mathbf{x},t')\left\langle G(\mathbf{x},t')|X'(\mathbf{x},t')=x'\right\rangle,\end{aligned} \tag{S14}$$

where $f(x';\mathbf{x},t)$ is the space-dependent vorticity PDF. Equation (S14) renders a conditional average, and the derivation has used Bayes' theorem. See Pope (2001) for the detailed algebra.

We rearrange the advection term by substituting in the velocity decomposition in (S9). As $\mathbf{U}_\omega$ is div-free, $\mathbf{U}_\delta$ is independent from f', and $\langle \nabla \cdot \mathbf{U}_\delta \rangle = \delta_0$, we get:

$$\begin{aligned} \left\langle \mathbf{U} \cdot \nabla f' \right\rangle &= \left\langle \mathbf{U}_\omega \cdot \nabla f' \right\rangle + \left\langle \mathbf{U}_\delta \cdot \nabla f' \right\rangle \\ &= \nabla \cdot \left\langle \mathbf{U}_\omega f' \right\rangle + \nabla \cdot \left\langle \mathbf{U}_\delta f' \right\rangle - \left\langle \nabla \cdot \mathbf{U}_\delta \right\rangle \left\langle f' \right\rangle \\ &= \nabla \cdot \left\langle \mathbf{U}_\omega f' \right\rangle + \nabla \cdot \left\langle \mathbf{U}_\delta f' \right\rangle - \delta_0 \left\langle f' \right\rangle . \end{aligned} \tag{S15}$$

The ensemble average PDF equation is:

$$\frac{\partial f}{\partial t'} = \frac{1}{\delta_0} \nabla \cdot \left\langle \mathbf{U}_\omega f' \right\rangle + \frac{1}{\delta_0} \nabla \cdot \left\langle \mathbf{U}_\delta f' \right\rangle - f - \frac{\partial}{\partial x'} \left(f \left\langle \frac{DX'}{Dt'} | X' = x' \right\rangle \right), \tag{S16}$$

Then, we implement an area average within MCS (denoted as $(\pi R^2)^{-1} \iint_{MCS} dS$) on (S10) to obtain the governing equation of $\sigma_c(x', t') = (\pi R^2)^{-1} \iint_{MCS} f dS$. Substitute (S11) into (S10), we get:

$$\frac{\partial \sigma_c}{\partial t'} + \frac{\partial F}{\partial x'} = -\sigma_c \quad \text{with} \quad F = \underbrace{\frac{1}{\pi R^2} \iint_{MCS} f \frac{\langle \delta | X' = x' \rangle}{\delta_0} dS}_{\text{updraft}} + \underbrace{\frac{\sigma_c}{\delta_0 \tau_d} (1 - e^{-x'})}_{\text{drag}}. \tag{S17}$$

Because $f' = 0$ outside the MCS and no vorticity patch has been observed to run out of the MCS due to the strong convergent flow, the $\nabla \cdot \langle \mathbf{U}_\omega f' \rangle$ and $\nabla \cdot \langle \mathbf{U}_\delta f' \rangle$ terms vanish after using Gauss theorem.

The probability current F consists of the drag part and the updraft part. The drag part pushes σ_c towards smaller ω_a and accumulates it there. The conditional average $\langle \delta | X' = x' \rangle$ in the updraft part is a bit obscure. As the updraft is homogeneously seeded in the MCS, $\langle \delta | X' = x' \rangle$ does not depend on $\mathbf{x}$, so the area average operator vanishes. Physically, $\langle \delta | X' = x' \rangle$ is contributed from a series of updraft events whose vorticity happen to cross x' at different phases of their lives. Thus, we need to know the instantaneous divergence at updraft area and how much they contribute to the x' bin. We define a "vorticity-equivalent" updraft divergence $\Delta x' / \widetilde{T}_u$ which characterizes the bulk vorticity growth during an updraft. By the start of an updraft, the r_u^2 / R^2 portion area of each x'

bin will be convective, and the total convective area distributed to that bin is proportional to its σ_c. Meanwhile, the temporal occupation of updraft is described by multiplying a $\widetilde{T_u}/\Delta t$ factor. Once an updraft starts, the convective area is fixed, but the x' within the updraft rises. The total divergent area contributed by these updrafts to x' must be normalized by the σ_c at x'. With these physical arguments, the updraft part becomes:

$$\begin{aligned}
&\frac{1}{\pi R^2}\iint_{MCS} f\frac{\langle\delta|X'=x'\rangle}{\delta_0}dS \\
&=\frac{\sigma_c(x',t)}{\delta_0}\left\langle\delta|X'=x'\right\rangle \\
&=\frac{\sigma_c(x',t)}{\delta_0}\left[\frac{1}{\sigma_c(x',t)}\frac{\Delta x'}{\widetilde{T_u}}\frac{r_u^2}{R^2}\int_{x'-\Delta x'}^{x'}\sigma_c\left(x'',t'-(x'-x'')\frac{-\delta_0\widetilde{T_u}}{\Delta x'}\right)\frac{\widetilde{T_u}}{\Delta t}dx''\right] \\
&\approx\frac{1}{\delta_0\Delta t}\frac{r_u^2}{R^2}\int_{x'-\Delta x'}^{x'}\left[\sigma_c\left(x',t'\right)-\frac{\partial\sigma_c}{\partial x'}|_{x',t'}(x'-x'')+\frac{1}{2!}\frac{\partial^2\sigma_c}{\partial x'^2}|_{x',t'}(x'-x'')^2+O(x'-x'')^3\right]dx'' \\
&=-D_1\sigma_c-\sum_{i=1}^{\infty}D_{i+1}\frac{\partial^i\sigma_c}{\partial x'^i},
\end{aligned} \tag{S18}$$

where D_i is shown in (31). On the fourth line, we have used Taylor expansion to approximate the contribution from other bins with derivative terms. The temporal part of Taylor expansion is neglected due to $-\delta_0\widetilde{\Delta\tau}\ll 1$. Larger $\Delta x'$ denotes more intermittent convection, which induces stronger nonlocality in PDF and therefore requires higher order cutoff in Taylor expansion. This result agrees with the modified equation of the Markov chain shown in (S7). Substitute (S18) into (S17), we obtain (28).

In the end, we derive the differential boundary condition at $x'=\Delta x'/2$, which is equivalent to the normalization condition. Integrate (28) from $x'=\Delta x'/2$ to $x'=+\infty$:

$$\int_{\Delta x'/2}^{\infty}\frac{\partial\sigma_c}{\partial t'}dx'=-\int_{\Delta x'/2}^{\infty}\sigma_c dx'-\int_{\Delta x'/2}^{\infty}\frac{\partial F}{\partial x'}dx'. \tag{S19}$$

Using the condition that F vanishes at $x' \to \infty$, we get the probability current at $x' = \Delta x'/2$ which renders a flux boundary condition there:

$$\frac{d}{dt'}\int_{\Delta x'/2}^{\infty} \sigma_c dx' = -\int_{\Delta x'/2}^{\infty} \sigma_c dx' + F|_{x'=\Delta x'/2} \Rightarrow F_0 = F|_{x'=\Delta x'/2} = -\frac{d\sigma_0}{dt'} + (1-\sigma_0)\,. \quad \text{(S20)}$$

Here $\sigma_0(t')$ is given in (27).

b. The analytical solution in $-\Delta h/H \to 0$ limit

The key is to find the asymptotic form of F_0. From Fig. 6b, we know $F_0 \to \infty$ as $t' \to 0$. We now prove it is a Dirac-Delta function at $t' = 0$. Let ε_0 be a small number that is sandwiched between $-\delta_0\tau_{\sigma_0} \ll \varepsilon_0 \ll 1$, where $-\delta_0\tau_{\sigma_0} = -\delta_0\Delta t/p$ is the rescaled adjustment time scale that is close to 0 for $-\Delta h/H \to 0$. The integral of F_0 within this small slot is calculated from (30):

$$\begin{aligned}\int_0^{\varepsilon_0} F_0 dt' &= \int_0^{\varepsilon_0} (1-p)^{-t'/(\delta_0\Delta t)} \frac{\ln(1-p)}{\delta_0\Delta t}\left(1+\frac{\delta_0\Delta t}{p}\right)dt' + \int_0^{\varepsilon_0}(1-\sigma_0)dt' \\ &\approx \frac{\ln(1-p)}{\delta_0\Delta t}\int_0^{\varepsilon_0}(1-p)^{t'/(-\delta_0\Delta t)}dt' + 0 \\ &= 1 - \left[(1-p)^{1/p}\right]^{\varepsilon_0/\tau_{\sigma_0}} \approx 1.\end{aligned} \quad \text{(S21)}$$

Here we have used $\sigma_0 \le 1$ to show the integral of $(1-\sigma_0)$ vanishes, and used $(1-p)^{1/p} \sim 0.3 < 1$ as a quite fixed value. Equation (S21) and $F_0(t'=0) \to \infty$ indicate that $F_0 \sim \Theta(t')$ for small t'. This, together with $F_0(t) \approx 1$ for larger t', constitute the expression of $F_0(t) = \Theta(t') + 1$. As for the PDF equation, we have $\lim_{-\Delta h/H \to 0} D_1 \to -1$. Other higher order coefficients vanish. Thus, the probability flux is $F = \sigma_c$. The full deterministic problem is:

$$\frac{\partial \sigma_c}{\partial t'} = -\frac{\partial \sigma_c}{\partial x'} - \sigma_c \quad \text{with} \quad \sigma_c|_{x'=0} = 1 + \Theta(t'). \quad \text{(S22)}$$

Its solution is shown in (33).

References

Durran, D. R., 2010: *Numerical methods for fluid dynamics: With applications to geophysics*, Vol. 32. Springer Science & Business Media.

Pope, S. B., 2001: *Turbulent flows*. IOP Publishing.

LIST OF TABLES

TABLE 1. List of symbols used in the paper

Symbol	Description	Value	Units
α_r	the link between "mass-equivalent" and "vorticity-equivalent" top-hat		
c_0	gravity wave speed		m s^{-1}
D_i	coefficients in the continuous PDF equation		
$\widetilde{D_i}$	the D_i that considers the discrete temporal stepping		
δ	divergence		s^{-1}
δ_0	average divergence within the MCS		s^{-1}
δ_0^+	δ_0 modified to consider the compensating divergence within the MCS		s^{-1}
δ_u	characteristic divergence within an updraft		s^{-1}
f_0	Coriolis parameter		s^{-1}
f'	the fine-grained vorticity PDF		
f	the space-dependent vorticity PDF		
F	probability current		
F_0	F at $x' = \Delta x'/2$		
g'	reduced gravity	0.72	m s^{-2}
h	layer thickness		m
H	basic state layer thickness	5×10^3	m
h'	disturbance layer thickness		m
$\widetilde{\Delta h}$	thickness loss in a "mass-equivalent" top-hat updraft		m
Δh	thickness loss in a "vorticity-equivalent" top-hat updraft		m
l_{diff}	the vorticity patch length scale for considering diffusion		m
L	domain width	800	km
L_R	Rossby deformation radius		m

Symbol	Description	Value	Units
ν	artificial viscosity		$m^2\ s^{-1}$
μ_m^n	the fraction of level m parcels at step n		
N	x and y direction grid point number	576	
ω	vertical relative vorticity		s^{-1}
ω_a	vertical absolute vorticity		s^{-1}
$\omega_{a,m}$	vertical absolute vorticity at level m		s^{-1}
$[\omega_a]^{r_u}$	the updraft end state mean ω_a within r_u		s^{-1}
$\overline{\omega}$	azimuthal average relative vorticity		s^{-1}
$\overline{\omega_p}$	resorted relative vorticity		s^{-1}
ω^+	mean ω within the MCS		s^{-1}
ω^-	mean ω outside of the MCS		s^{-1}
p	the probability for a parcel in the MCS to involve in an updraft		
ψ	stream function		$m^2\ s^{-1}$
Ψ	stream function as a random variable		$m^2\ s^{-1}$
ϕ	velocity potential		$m^2\ s^{-1}$
Φ	velocity potential as a random variable		$m^2\ s^{-1}$
Q_u	diabatic vertical velocity (mass sink) due to convection		$m\ s^{-1}$
Q_{rad}	diabatic vertical velocity (mass source) due to radiative cooling		$m\ s^{-1}$
Q_n	diabatic vertical velocity (mass sink) of the n^{th} updraft		$m\ s^{-1}$
$\widetilde{Q_m}$	peak diabatic vertical velocity of a “mass-equivalent” top-hat updraft		$m\ s^{-1}$
r_u	“vorticity-equivalent” top-hat updraft radius		m
$\widetilde{r_u}$	characteristic size of a Gaussian updraft		m
r_b	radius of solid body rotation core (only for the uniform forcing test)		m
r_m	radius of maximum azimuthal mean wind		m
r_{Um}	radius of maximum azimuthal mean wind of NAMI$\rightarrow 0$ profile		m
R	MCS radius	100	km
S^+	MCS area	πR^2	m^2
S^-	area outside of MCS	$L^2 - \pi R^2$	m^2

Symbol	Description	Value	Units
σ	the hybrid discrete-continuous PDF of $x' = \ln(\omega_a/f_0)$		
σ_0	the discrete part (basic level) of σ		
σ_c	the continuous part of σ		
σ_m^n	the discrete PDF at vorticity level m and time n		
σ_u	updraft fractional area		
t	time		s
t'	$t' = -\delta_0 t$ for a constant δ_0, or $t' = -\int \delta_0(t'')dt''$ for an extended problem		
t'_a	the sampling time for disorganized stage in the barotropic model		
t'_b	the sampling time for the vortex interaction stage in the barotropic model		
t'_c	the sampling time for the quasi-axisymmetric stage in the barotropic model		
t_A	roughly the MCS formation time in the 3D model		
t_B	A sampling time during the vortex developing stage in the 3D model		
t_C	Roughly the low-mid level convergence's peak time in the 3D model		
t'_B	nondimensionalized t_B (accumulated convergence)		
t'_C	nondimensionalized t_C		
t_n	peak time of the n^{th} updraft		s
τ_{rev}	characteristic time interval for two updrafts to hit on a fixed position		s
$\tau_{rev,m}$	the convective interval for a parcel to get involved in m updrafts during $-\delta_0^{-1}$.		s
τ_{σ_0}	adjustment time scale of σ_0		s
τ_d	Rayleigh drag time scale		s
τ_d^+	effective damping time scale that considers the inflow with negative vorticity		s
τ_{diff}	diffusion time scale of a vorticity patch		s
$\widetilde{\tau}_u$	characteristic duration time of a Gaussian updraft		s
$\widetilde{T}_u$	the duration time of a "mass-equivalent" top-hat updraft		s
Δt	updraft seeding time interval		s
$\Delta t'$	$\Delta t' = -\delta_0 \Delta t$		
$\Theta(t)$	Dirac-Delta function		s^{-1}/ none

Symbol	Description	Value	Units
θ_{00}	a reference potential temperature	300	K
$\mathbf{u}$	horizontal velocity vector		m s^{-1}
$\mathbf{U}$	horizontal velocity vector as a random variable		m s^{-1}
$\mathbf{U}_\omega$	vorticity-induced horizontal velocity vector as a random variable		m s^{-1}
$\mathbf{U}_\delta$	divergence-induced horizontal velocity vector as a random variable		m s^{-1}
u_{rb}	mean radial velocity at the MCS boundary		m s^{-1}
V_θ	azimuthal velocity		m s^{-1}
V_b	azimuthal velocity at r_b (only for the uniform forcing test)		m s^{-1}
V_{max}	maximum absolute wind		m s^{-1}
$\overline{V_m}$	maximum azimuthal mean wind		m s^{-1}
$V_U(r)$	the NAMI $\rightarrow$ 0 case radial profile of azimuthal velocity		m s^{-1}
V_{Um}	the maximum value of $V_U(r)$		m s^{-1}
$\mathbf{x}$	position vector		m
$\mathbf{x_n}$	position vector of the n^{th} updraft center		m
$\mathbf{x_n^*}$	initial position vector of the n^{th} updraft center		m
x'	nondimensional variable that depicts vorticity $x' = \ln(\omega_a/f_0)$		
X'	x' as a random variable		